



TiO₂-functionalized biochar from pistachio nutshells: adsorptive removal and photocatalytic decolorization of methyl orange

Ahmed S. El-Shafie¹ · Maha Abouseada¹ · Marwa El-Azazy¹

Received: 14 June 2023 / Accepted: 16 October 2023 / Published online: 6 November 2023
© The Author(s) 2023

Abstract

Pistachio nutshells-derived biochar (PNS-BC) was utilized as a cost-effective adsorbent for competently removing a model dye, methyl orange (MO) from wastewater. Three concentrations of TiO₂; 1%, 2%, and 3% were used to decorate the biochar. Analysis of morphology, stability, and structure of the three adsorbents (PNS, PNS-BC, and the TiO₂ functionalized biochar; TiO₂@PNS-BC) was extensively explored using various characterization techniques. The synergistic photocatalytic-adsorptive efficiency of the three adsorbents was compared. In this regard, a Box-Behnken (BB) design-based multivariate scheme was inaugurated with the target of maximizing MO removal (%R) while using the minimum possible of chemicals and resources. The impact of five variables; %TiO₂, dose of TiO₂-PNS, reaction time, dye concentration, and pH on the magnitude of %R was investigated. Results show that 97.69% removal of MO could be recognized over 120 min using adsorption compared to 99.47% removal over 30 min using 3% TiO₂@PNS-BC as a photocatalyst. A 3% TiO₂@PNS-BC was the best catalyst (compared to 1% and 2%) with a decolorization rate constant of 0.12741 min⁻¹, ~1.5 × faster compared to the decolorization of MO using adsorption alone. Adsorption of MO conformed well to Langmuir isotherm. A maximum adsorption capacity (q_{max}) of 142.38 mg/g was achieved. Adsorption kinetics fitted well with the pseudo-second order (PSO) model. Results obtained indicated that biochar of PNS is a promising, cost-effective, and economical adsorbent.

Keywords TiO₂-functionalized biochar · Pistachio nutshells · Methyl orange removal · Photocatalysis · Box-Behnken (BB) design

Introduction

Water plays an essential role in human life. Typically, the average daily use of water per person in developed countries exceeds 180 L per day. With the increase in population, the amount of water needed to grow food and livestock has significantly increased. The distribution of earth water comprises 97% saline water and only 3% fresh water (mostly icecaps). Only 30% of that fresh water is ground and surface water, which makes only 1% of water on earth fresh and accessible. Moreover, large amounts of fresh water are used for industry (20%) and irrigation (70%). For many reasons,

water has been contaminated by various pollutants that affect not only human health but the aquatic life as well (Goel 2006; Owa 2013).

Dyes are among the common aquatic pollutants. The existence of dyes in water does not only affect water's esthetic properties, but it also diminishes the light penetration into the stream disturbing the photosynthetic activity of the aqueous flora (El-Azazy et al. 2021a, b; El-Shafie et al. 2021). Methyl orange (MO) is a typical water-soluble azo dye that has been used in a plethora of applications. Yet, the most popular use of MO is as a pH indicator (Alardhi et al. 2023; Aljuaid et al. 2023; Iwuozor et al. 2021). The physicochemical properties of MO and its chemical structure are shown in Table S1.

Removal of MO has been accomplished using different approaches, such as advanced oxidation processes (Dai et al. 2023; Wang et al. 2023; Zhang et al. 2023), ultra-filtration (Yu et al. 2023), and electrochemical degradation (Leng et al. 2022; Wang et al. 2020a, b). Despite their effectiveness, these techniques are time consuming, require high cost,

Marwa El-Azazy and Ahmed S. El-Shafie have equally contributed to this work.

✉ Marwa El-Azazy
marwasaid@qu.edu.qa

¹ Department of Chemistry and Earth Sciences, College of Arts and Sciences, Qatar University, 2713, Doha, Qatar

and are sophisticated with limited applicability on a large scale (El-Azazy et al. 2021a, b; Iwuozor et al. 2021). In the same context, adsorption and photocatalysis were widely applied for synthetic dye removal. While each technique has its pros and cons, the cost-effectiveness, efficiency, scalability, and simplicity remain to be the most important features to judge the performance of either technique.

Surveying the literature shows that the adsorptive removal of MO has been achieved using various natural and synthetic adsorbents (Table S2). Natural adsorbents included biochar derived from coffee, and rice husks, wattle bark, lemon, orange, and banana peels (Annadurai et al. 2002; Bhatnagar et al. 2009; Cuong Nguyen et al. 2021; Loc et al. 2022; Yu et al. 2018). Synthetic adsorbents such as chitosan, and carbon nanotubes have also been used (Ahmad et al. 2017; Sui et al. 2012; Yao et al. 2011). By and large, the individual application of these techniques brings certain inadequacies such as a limited sportive capacity, poor photocatalytic efficiency, elevated regeneration costs, and the generation of secondary pollutants (Alardhi et al. 2023; Aljuaid et al. 2023; Bhatnagar et al. 2009; Chen et al. 2011; Da Dalt et al. 2013; El-Azazy et al. 2021a, b; El-Shafie et al. 2021; El Amri et al. 2023; Haque et al. 2010; Hidayat et al. 2023; Iwuozor et al. 2021; Loc et al. 2022; Zhang et al. 2021). Therefore, the development of a multifunctional “hybrid” material that can perform both as an adsorbent and photocatalyst remains a challenge.

Nevertheless, an efficient adsorbent serves to foster the photocatalytic degradation of the contaminant by accumulating the pollutant on the surface and hence increasing the contact with the photocatalyst. Moreover, in the hybrid material, the photoexcitation of electrons is usually followed by trapping of the excited electrons by the carbonaceous adsorbent. In the interim, the charge carriers will react with the adsorbed oxygen forming the superoxide radical reactive species, which in turn could be transferred to the adsorbed organic pollutant (either on the surface or inside the pores) fostering its degradation (Fito et al. 2022; Irani & Amoli-Diva 2020; Lim et al. 2011; Luo et al. 2019; Qiao et al. 2020; Shi et al. 2020; Yu et al. 2021).

Biochar (BC) – a carbonaceous material produced under oxygen-deficient conditions – is among the materials that have been commonly implemented in a nanocomposite photocatalyst (Fito et al. 2022; Lim et al. 2011; Yu et al. 2021). While BC can be produced from different sources, the BC sourced from biomasses and specifically agricultural wastes offers a renewable, cost-effective, and sustainable solution for several environmental challenges such as wastewater remediation via sensing, adsorptive removal, and photocatalytic degradation of pollutants (El-Azazy et al. 2023; El-Shafie et al. 2023; Ganesapillai et al. 2023; Lo Bello et al. 2022; Lu et al. 2022; Osman et al. 2022). Among the agro-wastes that are copiously produced and consumed

worldwide are nuts – sourced from argan, cashew, hazelnut, walnut, pecan, Macadamia, shea, pistachio, etc. Official reports show that 30×10^6 metric tons of pistachio nut waste is produced yearly from nuts processing industries with no fate other than incineration or landfill causing further pollution (Foo & Hameed 2011).

Photocatalysis using metal oxides (for instance titanium oxide TiO_2) for wastewater treatment has been widely explored, where TiO_2 possesses high stability and photoactivity. Yet, such an activity only appears under UV light with a high possibility of very fast electron–hole pair recombination suppressing the photoactivity. Moreover, the agglomeration and consequently the decrease in surface area, the wide band gap, the sluggish response for trace contaminants and complex wastewater matrices, and the production of toxic intermediates, are all limitations for single application of using TiO_2 as a photocatalyst (Fazal et al. 2020; Shan et al. 2020). Therefore, synthesis of hybrid materials with TiO_2 being loaded on the BC serves to resolve these glitches thanks to the oxygen functionalities-rich BC surface.

In the current approach, therefore, synthesis of TiO_2 @BC of pistachio nutshells (PNS) nanocomposites (TiO_2 @PNS-BC) will be employed to investigate the MO adsorptive-photocatalytic decolorization. Optimization of process variables will be approached via a multivariate-based conspiracy executing Box-Behnken (BB) response surface design and operating five independent parameters; % TiO_2 , dose of the nanocomposite (PNS-Ti), reaction time (RT), dye concentration [MO], and pH of the solution. Following such a scheme serves to alleviate the negative impact of chemicals on the environment via a reduced number of runs and producing trustworthy data (Akazdam et al. 2018; Box & Behnken 1960; El-Azazy, Kalla, et al. 2019a, 2019b; Farhan et al. 2021; Ferreira et al. 2007). A single dependent variable (%R) will be adjusted as a function of the 5 independent variables. Moreover, the structure of adsorbent is studied using numerous characterization techniques. The goal of this investigation is creating biochar with high efficiency, and low cost, via a sustainable approach.

Materials and methods

Chemicals

All chemicals were of high purity and were utilized as procured from the vendor (Sigma-Aldrich, USA) without further purification. Drugs used for testing the adsorbent selectivity (econazole nitrate, procaine hydrochloride, amantadine, raltegravir, and sulfisoxazole) were procured from Biosynth® Carbosynth Ltd. (UK). All investigations utilized deionized (DI, 18.2 MΩ cm) water acquired from

a Millipore-Q water system (Merck, USA). The waste left over from consuming local, unroasted, unsalted pistachio nuts was used to obtain pistachio nutshells (PNS). MO was procured from BDH Chemicals Ltd (UK). For batch adsorption studies, a 100 ppm stock solution of MO was prepared in DI water. Further dilutions were prepared in the same solvent.

Instrumentation: synthesis and characterization

PNS was initially dried using an oven (Mettler, Germany). Following this process, carbonization was performed in a Thermolyne™ furnace (USA). The obtained carbonized material was labeled as PNS-BC. The pH of the water in which the adsorbents were suspended was measured using a pH meter (Jenway 3305, UK). To change the pH levels, diluted aquatic solutions of HCl or NaOH were employed. A centrifuge (Thermo Fisher Scientific, USA) was used to help separating the adsorbent from the adsorbate. MO-adsorbent suspensions were filtered using nylon, 0.45 μm Millex membrane filters.

A UV–Vis spectrophotometer (Agilent diode-array, Agilent, USA) was used to determine the absorbance and, consequently, the quantity of MO in the filtrates using 10 mm matched quartz cuvettes. Photocatalysis experiments were performed using Spectroline® CM UV-viewing mini-cabinet with 4 W removable lamps (combination UV light source; 365 nm/254 nm), Sigma-Aldrich (USA). CHN elemental analysis was done using Thermo Scientific™ FLASH 2000 CHNS/O analyzer (USA). FT–IR spectroscopy was used to analyze the surface function groups of the tested adsorbents (Perkin Elmer, USA). A scanning electron microscope (SEM, FEI, Quanta 200, Thermo Fisher Scientific, USA) fitted with an energy-dispersive X-ray spectrometer (EDX) was used to study the morphologies and the elemental structure of the adsorbent. Raman spectroscopy was performed using a DXR Raman microscope (wavelength of 532 nm, 40 scans, and the laser power used is 9.2 mW using 50× microscope objectives, USA). The thermal stability of the prepared adsorbents was established using thermogravimetric analysis (TGA/dTA). Using an ASAP2020™ accelerated surface area and porosimetry system (Micrometrics, USA), surface features such as pore size, surface area, and volume were calculated. After degassing, N₂-adsorption and desorption were investigated. The isotherms recorded at 77 K were used to calculate the surface area and pore volume using the Brunauer–Emmett–Teller (BET) equation and *t*-plots and Barrett–Joyner–Halenda (BJH) equations. The BB design was created using Minitab®19 software (Minitab Inc., USA).

Preparation of pistachio nutshells (PNS)-based sorbents

Neither roasted nor salted pistachios were used, and the shells were peeled off, washed several times using tap water and a few times with DI water to eliminate dust and any residuals. Nutshells were dried in oven for 3 days at 80 °C (El-Azazy, El-Shafie, et al., 2019a, 2019b). Later, shells were pulverized using a non-metal blade blender to obtain powdered PNS which was sieved using a 125 mm sieve. Sieved powder was further split, one portion was labeled as PNS. The second portion was burned in a sealed crucible in the furnace for 60 min at 600 °C. The resultant material was placed in sealed vials and labeled as PNS-BC.

Synthesis of TiO₂@PNS-BC binary composites

Synthesis of TiO₂ nanoparticles was performed using the hydrothermal method. In this regard, a surfactant solution was employed to control the particle size. Therefore, 100 mL of 0.1 M of oleylamine dissolved in n-propanol was set aside stirring for 1 h and heated to 80 °C with fixed speed of 650 rpm. Thereafter, 68 mL of 0.09 M TiCl₄ solution was added, and pH of the solution was adjusted to 1.8 using 26% ammonia solution dropwise. The mixture was stirred for 2 h at 80 °C and 650 rpm. Later, the solution pH was adjusted to ~8 using 26% ammonia solution. After that, mixture was left at room temperature stirring for 20 h. Finally, the product went through centrifugation at 4000 rpm, washed with DI water, dried in the oven at 80 °C for dehydration overnight, and resultant product was labeled as TiO₂@PNS-BC (Marwa El-Azazy et al. 2021a, b).

Determination of the point-of-zero-charge (pH_{PZC})

To determine the pH_{PZC} of the three adsorbents (1%, 2%, and 3% of TiO₂@PNS-BC), an amount of 0.2 g of the former was mixed with 0.01 M NaCl aqueous solution in 50 mL volumetric flasks. The initial pH was adjusted to a pH value in the range of 2.00–10.00 ± 0.20 using aqueous solutions of 0.1 M NaOH or 0.1 M HCl. Samples were placed in the automatic shaker at 150 rpm for 48 h. Solutions were filtered and their final pH was measured. Graphs of final pH versus initial pH were plotted, and the pH_{PZC} value is determined as the intersection of the horizontal part of plot with the initial pH axis (Andas & Wazil 2019; Babić et al. 1999).

Batch adsorption experiments: box-behnken (BB) design

BB design was used to explore the impact of five variables on the dependent response variable, %R of MO, Table 1. Equation (1) is used to calculate %R of MO.

Table 1 Variables (independent and dependent) with their levels for the BB design

Variables and their codes		- 1	0	+ 1
(A)	Ti-impregnated %TiO ₂ , %TiO ₂	1%	2%	3%
(B)	Adsorbent dose (PNS-Ti), AD (mg/13 mL)	10	55	100
(C)	Reaction time, RT (min)	10	65	120
(D)	MO concentration, [MO] (ppm)	5	27.5	50
(E)	pH (pH unit)	2	6	10
Dependent variable		Removal percentage, %R		

$$\% R = 100 \times \frac{C_o - C_e}{C_o} \quad (1)$$

Where C_o and C_e symbolize the initial and equilibrium concentrations of dye [MO] (ppm), correspondingly. The experimental rehearsal as shown in Table 2 consisted of 46 experimental runs (including 6 central points, Ct Pt, level 0) performed over 2 blocks. For each experimental run, the scenario shown in Table 2 was followed and the %R was recorded. All runs were performed in triplicates and the average reading is noted. Response optimization was carried out using the individual desirability function (*d*) feature provided by Minitab®. Analysis of variance (ANOVA) was performed, and findings were compared to the quality tools used to assess the BB design. Regression paradigms were obtained and model features such as coefficient of determination (R^2), adjusted R^2 (R^2_{adj}), and predicted R^2 (R^2_{pred}) were noted and used to decide upon model linearity and prediction power. Predicted values are listed in Table 2. Calibration curves of different MO concentrations prepared at different pH values (Table 1) were constructed. The maximum wavelength (λ_{max}) for MO at pH = 6 and 10 is 462 nm, while at pH = 2 is 502 nm.

Equilibrium and kinetic investigations

To investigate the adsorption equilibrium, MO stock solution of 400 ppm was prepared. Further dilutions (1–200 ppm) of MO were prepared in DI water and the pH was adjusted using aqueous solution of 0.1 M HCl to 6.00 ± 0.20 . A blank was similarly prepared omitting MO. A mass of 0.100 ± 0.001 g of the adsorbent (3% TiO₂@PNS-BC) was then added to each tube. Later, the tubes were placed in automatic shaker at 150 rpm for 24 h. Solutions were filtrated, and absorbance of the sample was measured afterward at 462 nm. To study the adsorption kinetics, 0.500 ± 0.001 g of adsorbent (3% TiO₂@PNS-BC) was mixed with 150 mL of 100 ppm solution of MO, pH adjusted to 6.00 ± 0.20 . While stirring at 750

rpm at room temperature, and at different time intervals, aliquots of 10 mL were taken out over a total duration of 120 min. Solutions were filtered using 0.45 μ m filter, and absorbance was measured at 462 nm.

Photocatalytic degradation of MO: reaction kinetics

To test the efficiency of TiO₂@PNS-BC as a photocatalyst, an amount of 0.500 ± 0.001 g of the adsorbent (TiO₂@PNS-BC, with 1%, 2% and 3% of TiO₂) was mixed with 150 mL of 100 ppm aqueous solution of MO, then pH was adjusted to 6.00 ± 0.20 . Solutions were continuously stirred at 750 rpm while being irradiated using the UV lamp (short wavelength, 254 nm). During irradiation, aliquots of 10 mL were withdrawn, and filtered using 0.45 μ m syringe filter over a period of 120 min. Absorbances of the filtrates (average of triplicate measurements) were recorded at 462 nm. The experimental data were fitted to a second-order polynomial fitting.

The photocatalyst effectiveness was quantified with reference to its decolorization efficiency (%DE) toward MO, calculated using Eq. (2).

$$\% DE = 100 \times \frac{C_o - C_t}{C_o} \quad (2)$$

Where C_o symbolizes the initial [MO], while C_t denotes concentration of [MO] after a certain irradiation time, both expressed in ppm.

Adsorbent selectivity

The selectivity of 3% TiO₂@PNS-BC nanocomposite for MO was evaluated by equating the removal efficacy of 3% TiO₂@PNS-BC toward MO with its efficiency for eight other organic compounds including three dyes (methylene blue, rose bengal, basic fuchsin) and five drugs (econazole nitrate, procaine hydrochloride, amantadine, raltegravir, and sulfisoxazole) (Cantarella et al. 2019; El-Azazy et al. 2023). In this respect, volumes of 13 mL from each suggested pollutant (50 ppm aqueous solution) were

Table 2 BB design setup for the removal of MO

Run order	Block	Variables-independent					Variables-dependent	
		%TiO ₂ (A)	(PNS-Ti)AD (B)	RT (C)	[MO] (D)	pH (E)	%R _{Experimental}	%R _{Predicted}
01	1	2 (0)	10 (-)	65 (0)	27.5 (0)	2 (-)	46.90	46.67
02	1	2 (0)	55 (0)	120 (+)	50.0 (+)	6 (0)	49.98	52.08
03	1	2 (0)	55 (0)	10 (-)	50.0 (+)	6 (0)	13.03	15.21
04	1	3 (+)	10 (-)	65 (0)	27.5 (0)	6 (0)	10.04	7.69
05	1	1 (-)	10 (-)	65 (0)	27.5 (0)	6 (0)	2.00	1.93
06	1	2 (0)	55 (0)	65 (0)	50.0 (+)	10 (+)	25.67	20.83
07	1	2 (0)	55 (0)	65 (0)	27.5 (0)	6 (0)	73.99	74.63
08	1	3 (+)	55 (0)	120 (+)	27.5 (0)	6 (0)	63.15	57.19
09	1	2 (0)	100 (+)	65 (0)	27.5 (0)	2 (-)	80.17	72.99
10	1	2 (0)	100 (+)	65 (0)	27.5 (0)	10 (+)	84.81	78.98
11	1	1 (-)	100 (+)	65 (0)	27.5 (0)	6 (0)	4.78	5.87
12	1	2 (0)	55 (0)	65 (0)	27.5 (0)	6 (0)	73.46	74.64
13	1	2 (0)	55 (0)	65 (0)	5.0 (-)	2 (-)	74.73	77.70
14	1	2 (0)	55 (0)	65 (0)	5.0 (-)	10 (+)	70.58	72.01
15	1	2 (0)	10 (-)	65 (0)	27.5 (0)	10 (+)	6.36	6.73
16	1	1 (-)	55 (0)	10 (-)	27.5 (0)	6 (0)	1.33	0.85
17	1	2 (0)	55 (0)	65 (0)	50.0 (+)	2 (-)	73.06	66.11
18	1	1 (-)	55 (0)	120 (+)	27.5 (0)	6 (0)	3.63	3.92
19	1	2 (0)	55 (0)	120 (+)	5.0 (-)	6 (0)	80.80	72.05
20	1	3 (+)	55 (0)	10 (-)	27.5 (0)	6 (0)	22.44	16.38
21	1	2 (0)	55 (0)	65 (0)	27.5 (0)	6 (0)	74.83	74.64
22	1	2 (0)	55 (0)	10 (-)	5.0 (-)	6 (0)	57.63	52.33
23	1	3 (+)	100 (+)	65 (0)	27.5 (0)	6 (0)	97.69	95.02
24	2	2 (0)	55 (0)	65 (0)	27.5 (0)	6 (0)	78.46	74.64
25	2	2 (0)	10 (-)	65 (0)	50.0 (+)	6 (0)	15.43	13.75
26	2	1 (-)	55 (0)	65 (0)	50.0 (+)	6 (0)	6.01	5.75
27	2	3 (+)	55 (0)	65 (0)	50.0 (+)	6 (0)	22.21	25.37
28	2	1 (-)	55 (0)	65 (0)	27.5 (0)	10 (+)	2.52	3.33
29	2	2 (0)	100 (+)	65 (0)	50.0 (+)	6 (0)	62.24	69.24
30	2	2 (0)	100 (+)	120 (+)	27.5 (0)	6 (0)	92.96	92.57
31	2	2 (0)	55 (0)	65 (0)	27.5 (0)	6 (0)	69.84	74.64
32	2	3 (+)	55 (0)	65 (0)	27.5 (0)	10 (+)	19.11	25.62
33	2	3 (+)	55 (0)	65 (0)	27.5 (0)	2 (-)	65.26	66.05
34	2	2 (0)	55 (0)	10 (-)	27.5 (0)	2 (-)	26.36	33.03
35	2	2 (0)	100 (+)	10 (-)	27.5 (0)	6 (0)	39.52	38.82
36	2	2 (0)	100 (+)	65 (0)	5.0 (-)	6 (0)	94.80	100.25
37	2	2 (0)	55 (0)	65 (0)	27.5 (0)	6 (0)	77.40	74.64
38	2	2 (0)	55 (0)	10 (-)	27.5 (0)	10 (+)	20.39	20.11
39	2	2 (0)	10 (-)	120 (+)	27.5 (0)	6 (0)	16.13	20.37
40	2	2 (0)	55 (0)	120 (+)	27.5 (0)	2 (-)	68.91	75.98
41	2	1 (-)	55 (0)	65 (0)	5.0 (-)	6 (0)	7.97	8.91
42	2	2 (0)	10 (-)	10 (-)	27.5 (0)	6 (0)	8.25	11.11
43	2	1 (-)	55 (0)	65 (0)	27.5 (0)	2 (-)	9.36	7.05
44	2	2 (0)	55 (0)	120 (+)	27.5 (0)	10 (+)	39.86	37.02
45	2	2 (0)	10 (-)	65 (0)	5.0 (-)	6 (0)	48.96	43.84
46	2	3 (+)	55 (0)	65 (0)	5.0 (-)	6 (0)	72.50	81.99

mixed with 0.100 ± 0.005 g of 3% TiO_2 @PNS-BC. The pH of the solution was then adjusted to 6.00 ± 0.20 using 0.1 M aqueous solution of HCl. The mixture was stirred at 150 rpm for 30 min. Samples were filtered, and the filtrate absorbance was recorded at λ_{max} of each pollutant solution.

Results and discussion

Characterization of the as-prepared adsorbents

SEM and EDX analyses

The morphology and the composition of the prepared binary composites were evaluated using SEM and EDX techniques. The SEM micrographs of the PNS-BC sample in Fig. 1a, b confirmed the presence of pores with different sizes that could aid in the removal of the studied dye. At a higher magnification, the pores of PNS-BC resemble a honeycomb showing the capability of the BC to uptake MO. Furthermore, the SEM micrographs of the samples loaded with TiO_2 nanoparticles showed an increase in the existence of nanoparticles on the surface, which was proportional to the amount of loaded TiO_2 . Specifically, Fig. 1d, e shows a small amount of TiO_2 nanoparticles on the surface of the PNS-BC for the 1% TiO_2 @PNS-BC sample, while Fig. 1g, h reveals an increase in the existence of nanoparticles on the surface for the 2% TiO_2 @PNS-BC sample. Finally, Fig. 1j, k shows a heavy existence of TiO_2 nanoparticles which have covered almost all the surface and the pores of the PNS carbonaceous material in the case of 3% TiO_2 @PNS-BC sample.

The findings from the SEM micrographs were supported by the EDX analysis in Fig. 1c, f, i, and m. The data showed a decrease in carbon concentration from 88.74% for PNS-BC to 81.84% in 3% TiO_2 @PNS-BC due to the presence of TiO_2 on the surface. In contrast, the oxygen concentration on the surface increased from 10.71% in PNS-BC to 14.73% in 3% TiO_2 @PNS-BC due to the formation of metal oxide on the surface. The presence of titanium was confirmed by an increase in titanium concentration from 1.20% in 1% TiO_2 @PNS-BC to 3.29% in 3% TiO_2 @PNS-BC, thereby confirming the successful preparation of different concentrations of TiO_2 loaded-PNS-BC.

CHN analysis

Table 3 presents the results of the CHN analysis conducted on the as-prepared samples. According to the data, the %N increased from 0.02% for PNS-BC to 0.08% for 3% TiO_2 @PNS-BC, which could be attributed to the use of oleylamine in the synthesis of TiO_2 nanoparticles. Similarly, the H% increased from 1.45% in PNS-BC to 2.64% in 3% TiO_2 @PNS-BC. However, the percentage of C% decreased from

87.40% in PNS-BC to 70.05% in 3% TiO_2 @PNS-BC due to the presence of TiO_2 on the surface, as confirmed previously using SEM and EDX analyses.

Raman spectroscopy and TGA analyses

Raman analysis was employed to study the structure of as-prepared TiO_2 @PNS-BC binary composites, as illustrated in Fig. 2a. The obtained spectra exhibited the representative Raman modes; the characteristic peaks of the anatase phase of TiO_2 (active form), including the E_g mode at 139 cm^{-1} , B_{1g} mode at 412 cm^{-1} , B_{1g}/A_{1g} at 549 cm^{-1} , and the E_g mode at 638 cm^{-1} . The obtained data agrees with the reported data for the previously prepared anatase TiO_2 nanoparticles (Antonio-Cisneros et al. 2015; Pang et al. 2021; Yu et al. 2014). Figure 2a also showed the presence of two strong bands at 1361 cm^{-1} , which corresponds to a D band which is associated with the presence of sp^3 C–C atoms, and the second band at 1595 cm^{-1} , known as the graphitic band, related to the E_{2g} phonon of the sp^2 carbon (C=C) atoms, and both are characteristic peaks of carbonaceous materials (Beams et al. 2015; Fernández-Ibáñez et al. 2015). Additionally, the I_D/I_G ratio decreased from 0.67 in PNS-BC to 0.63 in 3% TiO_2 @PNS-BC, indicating that the number of defects on the biochar surface decreased after loading of TiO_2 nanoparticles, which could potentially affect the adsorption and photocatalytic activity of the prepared binary composites.

The TGA/dTA analysis for the two samples, PNS-BC and 3% TiO_2 @PNS-BC, is shown in Fig. 2b. The results indicate that both binary composites exhibited weight loss between 50 and 250 °C (16.49% for PNS-BC and 21.48% for 3% TiO_2 @PNS-BC), which can be attributed to the loss of surface-free water. Furthermore, a second weight loss was observed in the temperature range of 460–800 °C, with PNS-BC and 3% TiO_2 @PNS-BC showing weight losses of 30.18% and 22.48%, respectively. This could be due to the loss of organic matter and the carbonization of the polymeric components in the carbonaceous material. The final weight loss for PNS-BC was 51.95%, and for 3% TiO_2 @PNS-BC, it was 55.87%, with a difference of 3.92%, representing the amount of TiO_2 nanoparticles impregnated onto the PNS-BC. Moreover, the presence of TiO_2 nanoparticles on the surface of the biochar enhances the thermal stability of the prepared nanosorbent.

FT-IR analysis and point-of-zero-charge (pH_{pzc})

The FT-IR assignments for the as-prepared PNS-BC samples before and after loading with different concentrations of TiO_2 nanoparticles show the presence of significant functional groups that could participate in removing MO from wastewater. The IR spectrum, Fig. 3a reveals the presence of several peaks in the TiO_2 -impregnated sample and during

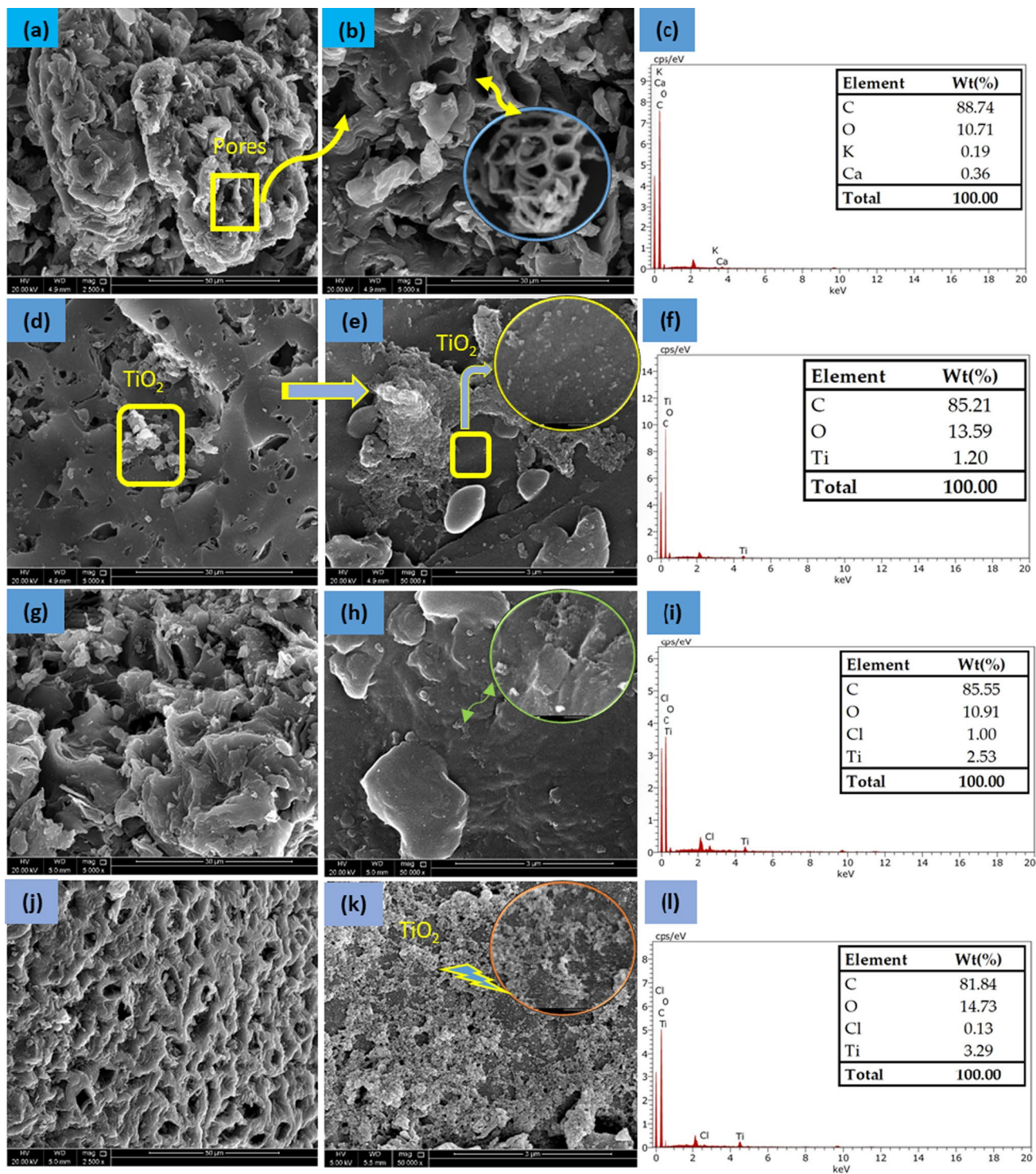


Fig. 1 SEM graphs of **a, b** PNS-BC, **d, e** 1% TiO₂@PNS-BC, **g, h** 2% TiO₂@PNS-BC, **j, k** 3% TiO₂@PNS-BC at different magnifications, **c, f, i, m** EDX analyses of PNS-BC, 1% TiO₂@PNS-BC, 2% TiO₂@PNS-BC, and 3% TiO₂@PNS-BC, respectively

the preparation process. These peaks include the absorption band at 2928 cm⁻¹, corresponding to the stretching vibration of aliphatic C–H (methylene) bonds, a characteristic feature of carbonaceous materials. The peak at 2845 cm⁻¹

corresponds to aliphatic C–H stretching vibrations, while the absorption peak at 1045 cm⁻¹ is often associated with the stretching vibration of C–O or C–N bonds in carbonaceous materials and it can be also attributed to the bending

Table 3 CHN analysis of PNS-BC before and after loading of different concentrations of TiO₂ (1%, 2% and 3% TiO₂)

Adsorbent	N (wt%)	C (wt%)	H (wt%)
PNS-BC	0.02	87.40	1.45
1% TiO ₂ @ PNS-BC	0.04	81.21	2.54
2% TiO ₂ @ PNS-BC	0.06	75.39	2.36
3% TiO ₂ @ PNS-BC	0.08	70.05	2.64

vibration of the Ti–OH (León et al. 2017; Mugundan et al. 2015). Furthermore, the absorption band at 873 cm⁻¹ corresponds to the bending vibration of Ti–O–Ti bonds in titanium oxide, confirming the presence of TiO₂ on the surface of PNS-BC (Lu et al. 2019; Marwa et al. 2022; Pang et al. 2021).

On the other hand, the remaining peaks in the spectrum are related to carbonaceous materials and appear in all the as-prepared samples. For instance, the peak at 2163 cm⁻¹ is attributed to the stretching vibration of a C≡C triple bond, often present in certain carbonaceous materials. The band at 1961 cm⁻¹ may be assigned to the stretching vibration of a carbonyl functional group (C=O) on the surface of PNS-BC carbonaceous material. Additionally, the absorption peak at 1561 cm⁻¹ is related to the stretching vibration of C=C bonds in aromatic structures, which can be present in carbonaceous materials.

The surface charge of the studied nanosorbents was investigated, and the obtained data revealed that the pH_{PZC} of PNS-BC was 6.34 ± 0.20. After loading with TiO₂ nanoparticles, the pH_{PZC} values for 1% TiO₂@PNS-BC, 2% TiO₂@PNS-BC, and 3% TiO₂@PNS-BC were 4.87, 5.11, and 5.08 ± 0.20, respectively, Fig. 3b. These figures indicate that the surface of the as-prepared adsorbents has more acidic functional groups, which could positively affect the removal efficiency of the studied adsorbents. Furthermore, the surface of 3% TiO₂@PNS-BC is positively charged at pH values lower than 5.08 ± 0.20 and negatively charged at pH values higher than 5.08 ± 0.20.

Analysis of the surface area and pore size

The results of the BET analysis for PNS-BC and 3% TiO₂@PNS-BC are presented in Fig. 4a–d and Table 4. The obtained data reveals that the multi-point BET surface area (SA) for PNS-BC and 3% TiO₂@PNS-BC were 5.77 m²/g and 33.37 m²/g, respectively. The acquired data confirms that the surface area of PNS-BC has increased with the addition of TiO₂ nanoparticles. The increase in the surface area directly affects the adsorption efficiency of 3% TiO₂@PNS-BC toward MO. The single point total pore volume decreased from 0.168 cm³/g in PNS-BC to 0.028 cm³/g in 3% TiO₂@PNS-BC due to the coverage of most pores on

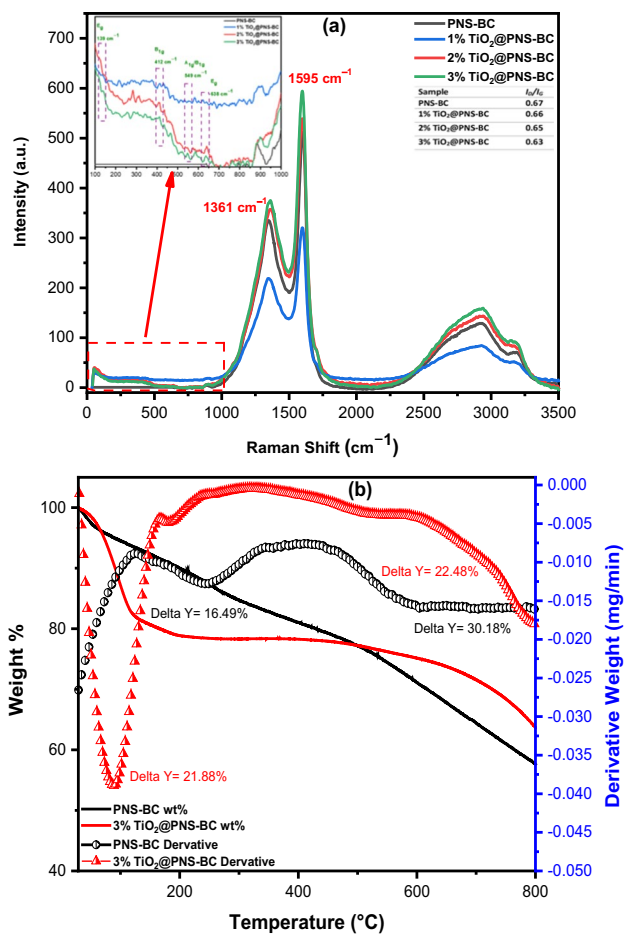


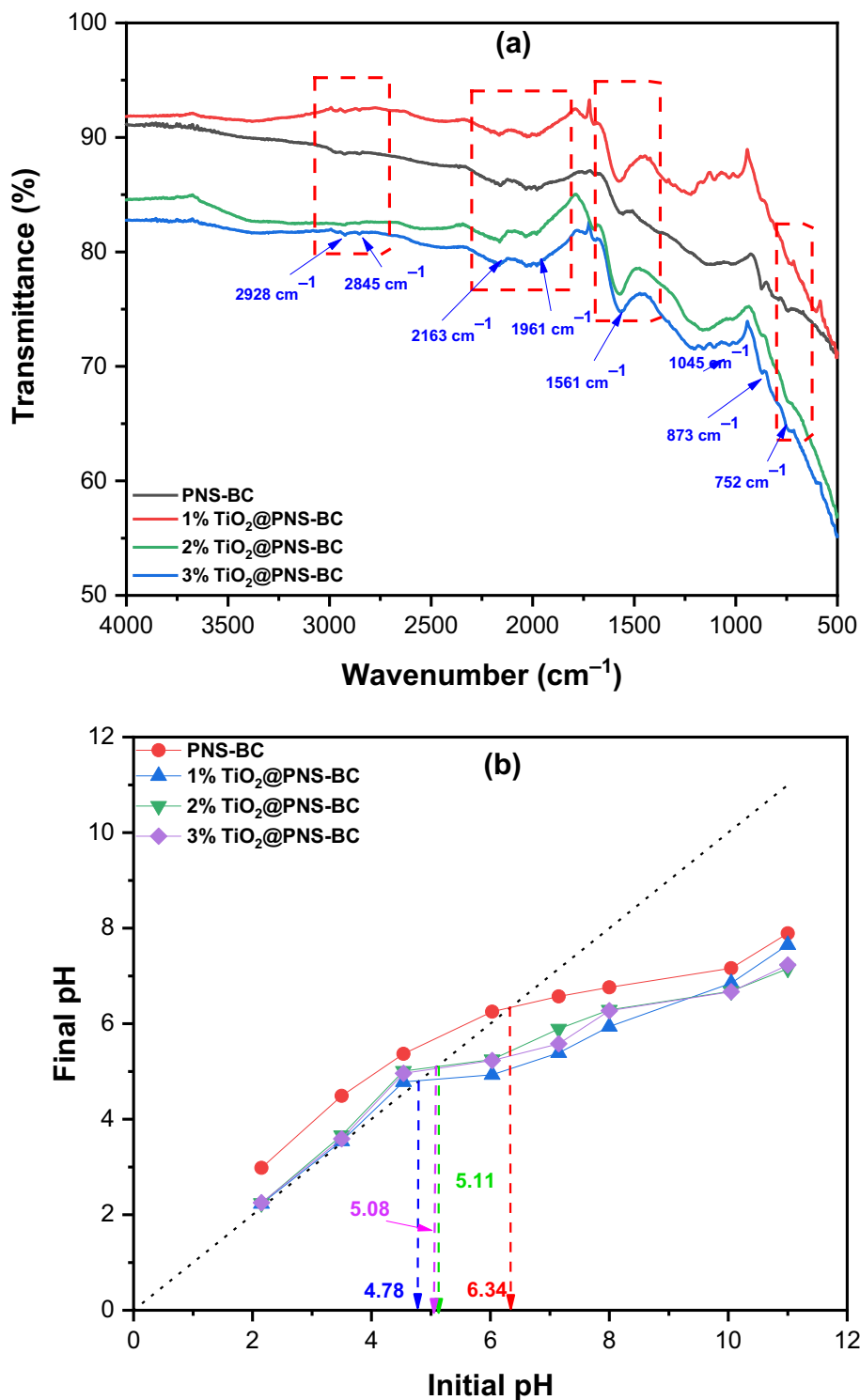
Fig. 2 **a** Raman spectra of the as-prepared samples including PNS-BC, 1% TiO₂@PNS-BC, 2% TiO₂@PNS-BC, and 3% TiO₂@PNS-BC, **b** TGA/dTA analysis for PNS-BC and 3% TiO₂@PNS-BC

the surface of the PNS-BC with the TiO₂ nanoparticles, as observed from the SEM micrographs. Additionally, both samples contained two types of pores: mesopores with pore sizes ranging from 2 to 50 nm and macropores with pore sizes greater than 50 nm, Fig. 4b and d. Figure 4a, c shows that the adsorption isotherm and hysteresis loop for both samples is of type IV and H3 form, which is characteristic of porous carbonaceous materials.

X-ray diffraction (XRD) analysis

Performing XRD analysis is crucial for identifying the crystalline phase of powdered materials. In this study, the samples were subjected to X-ray diffraction analysis to confirm the crystalline phase of the as-prepared PNS-BC before and following the loading of TiO₂ nanoparticles. Figure 5 depicts the XRD diffractogram patterns of the prepared samples, namely PNS-BC, 1% TiO₂@PNS-BC, 2% TiO₂@PNS-BC, and 3% TiO₂@PNS-BC. The XRD pattern of the PNS-BC sample shows a broad peak

Fig. 3 FT-IR spectrum of **a** as-prepared samples including PNS-BC, 1% TiO₂@PNS-BC, 2% TiO₂@PNS-BC, and 3% TiO₂@PNS-BC, **b** p*H*_{PZC} for the four samples



between 2θ : 15° and 30°, indicating the amorphous state of the PNS-BC. This peak was also present in TiO₂@PNS-BC, indicating the presence of a carbon layer with TiO₂ nanoparticles (Elamin et al. 2023; Pravakar et al. 2021).

Furthermore, the XRD pattern, Fig. 5 of the as-prepared TiO₂@PNS-BC reveals two small peaks at 28°, 34°, 40°, 50°, and 58°, which could be corresponding to the (101), (004), (200), (105), and (211) planes, respectively

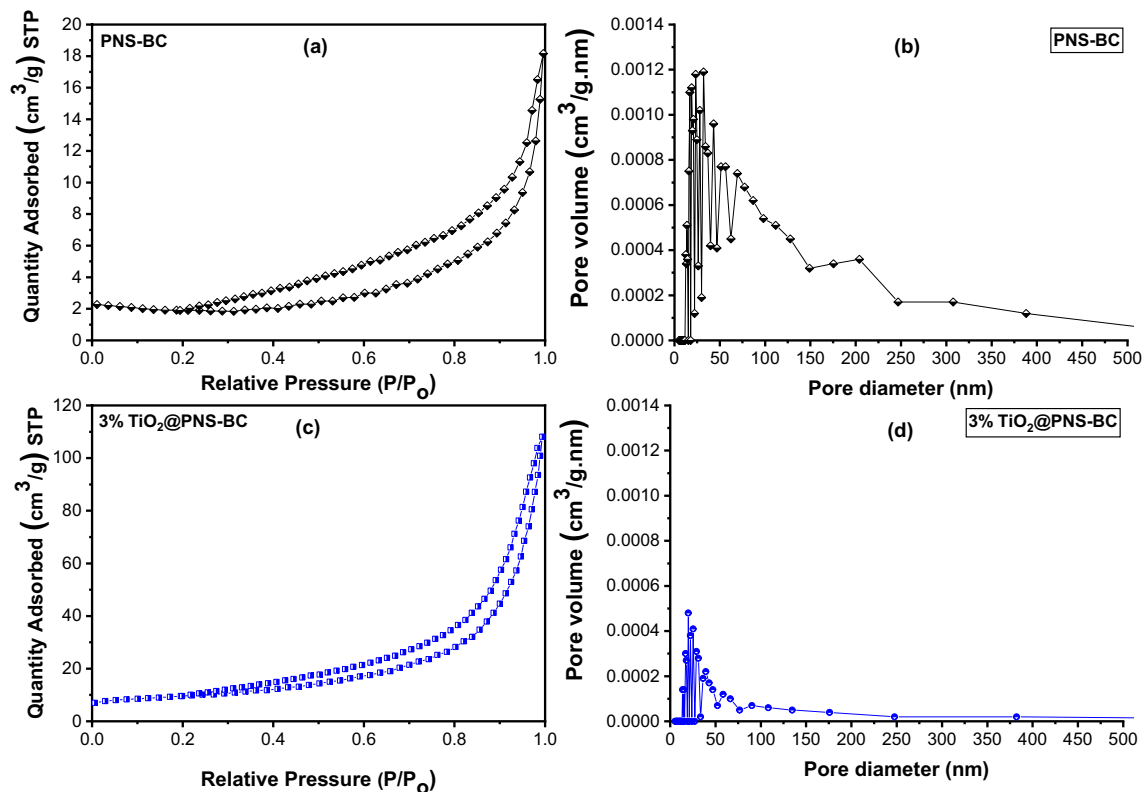


Fig. 4 Nitrogen adsorption–desorption isotherms for **a** PNS-BC, **c** 3% TiO₂@PNS-BC and the pore diameter for **b** PNS-BC, **d** 3% TiO₂@PNS-BC

(ICSD: 01–089) (Wang et al. 2020a, b). These characteristic planes confirm the presence of TiO₂ nanoparticles in the anatase phase, which agrees with the Raman analysis findings.

BB design analysis: quality charts and ANOVA

BB design is a response surface methodology (RSM)–based design. This design requires three levels for each parameter, highest (+1) and lowest (–1) (Box & Behnken 1960; El-Azazy, Kalla, et al., 2019a, 2019b; Ferreira et al. 2007; Tripathi et al. 2009). One of the advantages of the BB design is that for all experiments needed, none of the experiments contain a combination where all factors are neither at

the highest nor at the lowest levels. This is done to avoid extreme conditions in the generated set of experiments, as that may result in undesirable results.

In the current investigation, removal of MO was studied as a function of 5 variables. Pareto chart, Fig. 6a was used to demonstrate the variables' significance. In this study, the most significant variables were the squared effect of the %TiO₂ (AA). On the other hand, pH (E) had the lowest influence on %R among all studied main effects. As also revealed by the Pareto chart, variable-variable interactions such as BD (AD and [MO]), and CE (RT and pH) had the most statistically insignificant effect on the removal of MO. Figure 6b shows the contour plots depicting the data in a 2D format. The dark red zones designate regions with the lowest %R of MO, in contrast to the dark gray areas.

Analogous inferences could be drawn from the ANOVA performed at 95.0 confidence interval. Acquired results – not shown, reveals that terms with *p*-value < 0.05 are statistically significant.

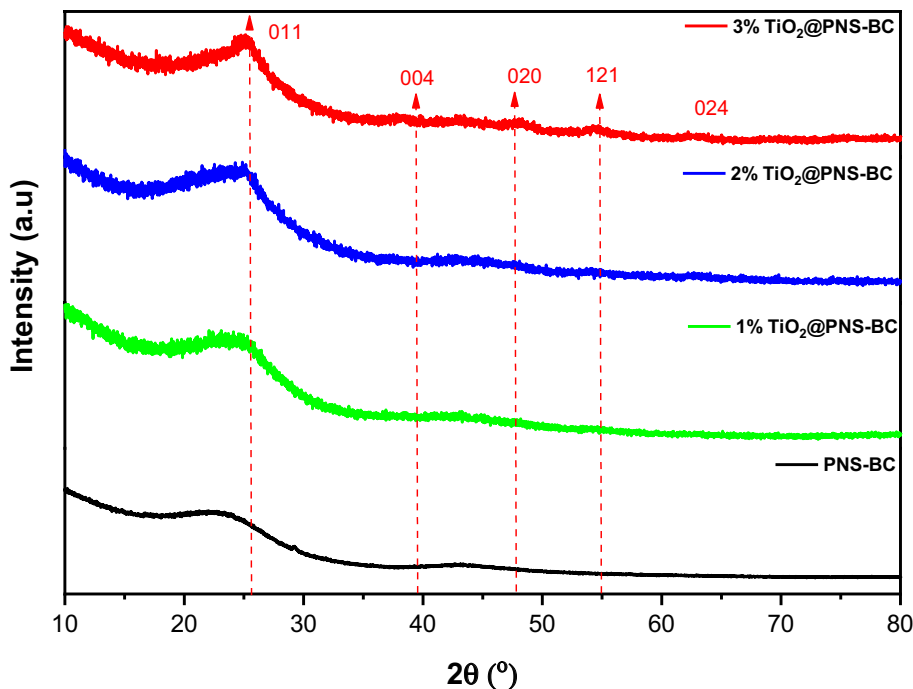
Table 4 Collected BET analysis data for PNS-BC and 3% TiO₂@PNS-BC

Parameters	PNS-BC	3% TiO ₂ @PNS-BC
Multi-point BET SA (m ² /g)	5.77	33.37
Single point total pore volume (cm ³ /g)	0.168	0.028
Single point average pore radius (Å)	100.8	98.0

Regression equation

Regression model in terms of coded variables is given by Eq. (4). In addition to showing the magnitude of each effect

Fig. 5 Powder XRD pattern of PNS-BC, 1% TiO₂@PNS-BC, 2% TiO₂@PNS-BC, and 3% TiO₂@PNS-BC



(whether main, squared or variable-variable interactions), the regression model shows the direction of the effect on the measured response. To find the overall impact of any term, the total contribution of such term should be considered.

$$\begin{aligned} \sqrt{\%R} = & -13.23 + 15.226A - 0.0212B + 0.0521C + 0.0728D \\ & + 0.631E - 3.426A^2 - 0.000558B^2 - 0.000524C^2 \\ & - 0.00068D^2 - 0.04974E^2 + 0.03301AB + 0.01118AC \quad (3) \\ & - 0.03813AD - 0.1397AE + 0.000223BC + 0.000302BD \\ & + 0.00636BE + 0.000417CD - 0.001556CE - 0.00899DE \end{aligned}$$

In this regard, the values of R^2 and R^2_{adj} were 98.81% and 97.77%, respectively, which are high enough to confirm the goodness-of-fit and the good linearity. While R^2_{pred} was found to be 95.08%, which confirms a good prediction power for new observations.

Optimization phase

As the aim of this investigation is to maximize the removal of MO, the individual desirability function (d) value was used to decide upon the optimum adsorption conditions. Acquired results show that a factorial combination of %TiO₂ \approx 3% (a plateau started at \sim 2.7%), AD = 78.11 mg/13 mL, RT = 120 min, [MO] = 5 ppm, and pH = 5.74 could achieve the target which is the maximum removal of MO as reflected by the high value of the d function. Optimum conditions were further utilized for all subsequent experiments.

Equilibrium and kinetics investigations

To investigate the MO adsorption process, the adsorption isotherms were used to estimate the amount of MO accumulation on the adsorbent surface and the type of interaction of MO-adsorbent. Adsorption of MO onto 3% TiO₂@PNS-BC at a constant temperature was studied using four equilibrium isotherms; Langmuir, Freundlich, Temkin, and Dubinin–Radushkevich (D–R) (Araújo et al. 2018; Guo & Wang 2019; Langmuir & Herman 1980; Moussavi & Barikbin 2010).

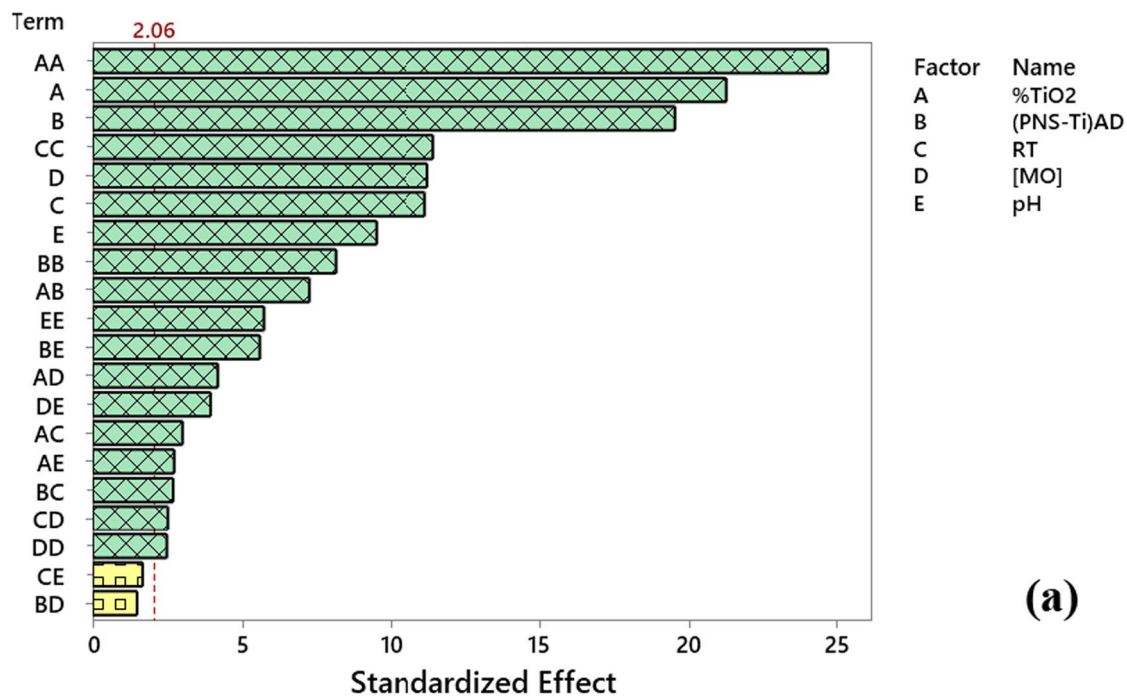
The Langmuir isotherm frequently suggests one of the following three main hypotheses:

- (i) The adsorption sites have identical adsorption energy,
- (ii) The adsorbate molecule occupies only one site on the surface, and there is no interaction between the adsorbate molecules,
- (iii) The adsorption is mostly confined to the adsorbent surface.

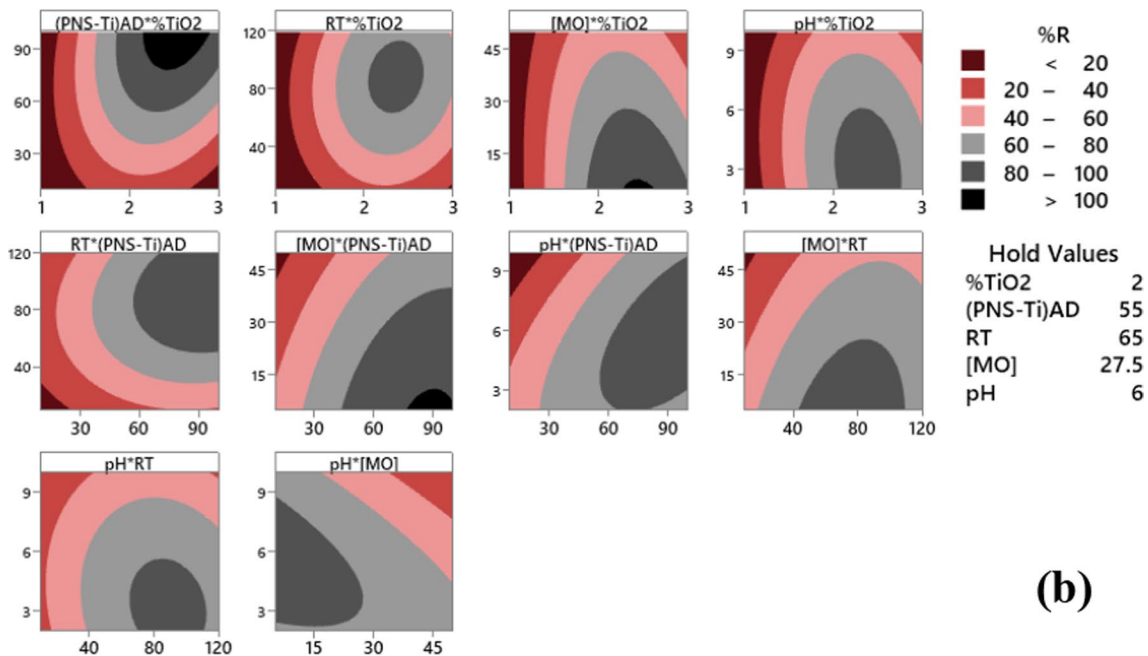
Equation (4) was used to demonstrate the Langmuir isotherm as follows:

$$q_e = \frac{q_m K_L C_e}{1 + K_L C_e} \quad (4)$$

where q_m and K_L represent the maximum adsorption capacity (mg/g) and Langmuir equilibrium coefficient (L mole⁻¹),



(a)



(b)

Fig. 6 a Pareto chart of standardized effect, b 2D-contour plots

respectively. Moreover, Langmuir model can be expressed using Langmuir equilibrium coefficient as shown in Eq. (5).

$$R_L = \frac{1}{1 + K_L C_0} \tag{5}$$

Thus, R_L and C_0 refer to the separation factor and initial concentration of MO, respectively. The R_L is used to

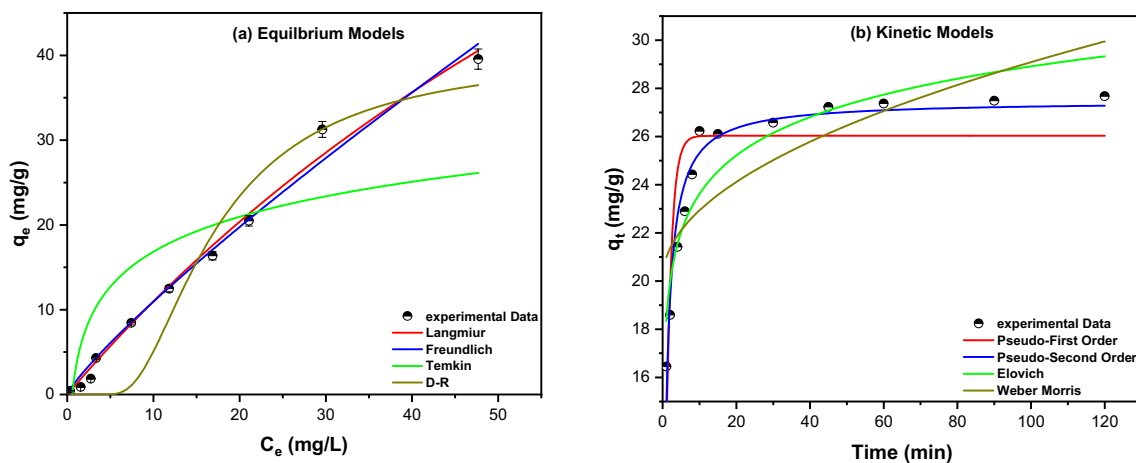


Fig. 7 a Equilibrium models including Langmuir, Freundlich, Temkin, D-R, b kinetic models including PFO, PSO, Elovich and Weber Morris for the adsorption of MO onto 3% TiO₂@PNS-BC

Table 5 Equilibrium and kinetic models for the adsorption of MO onto 3% TiO₂@PNS-BC

Model	Nonlinear equations	Parameters	Value
Langmuir	$q_e = \frac{q_m K_L C_e}{1 + K_L C_e}$	q_m (mg/g)	142.38
		K_L (L. mole ⁻¹)	0.0083
		R ²	0.9913
Freundlich	$q_e = K_F C_e^{1/n}$	1/n	0.85
		K_F (mole/g) (L/mole) ^{1/n}	1.544
		R ²	0.9874
Temkin	$q_e = \frac{RT}{b_T} \ln(A_T C_e)$	b_T (J/mole)	416.06
		A_T (L/mole)	1.69
		R ²	0.6969
D-R	$q_e = q_s \cdot \exp(-\beta \cdot \epsilon^2)$ $\epsilon = RT(1 + \frac{1}{C_e})$ $E = 1/\sqrt{2\beta}$	β	7.42 × 10 ⁻⁸
		E (kJ/mole)	2.59
		q_m (mg/g)	40.26
		R ²	0.9311
Pseudo-first order (PFO)	$\frac{dq_t}{dt} = k_1(q_e - q_t)$	K_1 (min ⁻¹)	0.713
		q_e (mg/g)	26.03
		R ²	0.7466
Pseudo-second order (PSO)	$\frac{dq_t}{dt} = k_2(q_e - q_t)^2$	K_2 (g.mg ⁻¹ .min ⁻¹)	0.043
		q_e (mg/g)	27.47
		R ²	0.9531
Elovich model	$q_t = \frac{1}{\beta} \times \ln(1 + \alpha\beta t)$	α	6705
		β	0.435
		R ²	0.8659
Weber Morris model	$q_t = K_1 t^{0.5} + C$	K_1	0.8999
		C	20.08
		R ²	0.6188

q_m maximum adsorption capacity, K_L Langmuir constant, K_F , 1/n Freundlich constants, A_T , b_T Temkin constants, R universal gas constant, T temperature, q_s saturation capacity, β activity coefficient, and ϵ calculated Polanyi potential, q_t capacity at t , K_1 adsorption rate constant, t adsorption time, K_2 adsorption rate constant, α , β Elovich constants, K_1 intraparticle diffusion rate constant, C thickness of the boundary layer

determine the desirability of the adsorption process, thus, if calculated R_L is = 1 then the adsorption process is unfavorable, while if R_L value is between 0 and 1, then the process is favorable and spontaneous. If $R_L = 0$, the reaction is considered irreversible. The determined value (Fig. 7a and Table 5) of R_L for MO onto 3% TiO₂@PNS-BC was < 1, denoting that the adsorption process is favorable, and happened spontaneously. Moreover, the adsorption of MO became irreversible when [MO] was high. The calculated parameters in Table 5 show that the maximum adsorption capacity for MO was 142.38 mg/g. The resultant data indicates that the adsorption of MO onto 3% TiO₂@PNS-BC fit well with the Langmuir isotherm with $R^2 = 0.9913$. The obtained data confirms that the adsorbent (3% TiO₂@PNS-BC), has high adsorptive capability toward MO.

The Freundlich isotherm, on the other hand, is a useful tool for describing the energy of a heterogeneous surface, as shown by Eq. (6):

$$q_e = K_F C_e^{\frac{1}{n}} \quad (6)$$

where C_e is [MO] at equilibrium (mg/L), q_e is amount of MO adsorbed per unit mass (mg/g), K_F (mole.g⁻¹) (L.mole⁻¹), and $1/n$ is Freundlich coefficient that determines the adsorbent capacity and the change in its intensity, in addition to the deviation from linearity. The calculated parameters in Table 5 show that the Freundlich coefficient $1/n = 0.85$, and $n = 1.176$. As a result, the adsorption potential calculated using Eq. (7) = 2.913 kJ, meaning that all MO molecules with potential energy < 2.913 kJ will be adsorbed onto 3% TiO₂@PNS-BC. Besides, the MO adsorption process will be favorable and irreversible.

$$A = n R T \quad (7)$$

Temkin isotherm is the model used to describe the interaction between adsorbent and adsorbate and can be illustrated using the following Eq. (8):

$$q_e = \frac{RT}{b_T} \ln(A_T C_e) \quad (8)$$

Where R is the universal gas constant (8.314 J/mol.K), T is the temperature (K), b_T quantifies the sorption energy, and A_T is the Temkin isotherm equilibrium binding constant. According to Fig. 7a and Table 5, MO has sorption energy is 416.06 J/mol. The obtained results suggest that MO adsorbs favorably on the surface of 3% TiO₂@PNS-BC adsorbent, these results confirm the Langmuir and Freundlich findings.

Dubinin–Radushkevich (D–R) isotherm was studied at room temperature to determine the adsorption mechanism of MO on 3% TiO₂@PNS-BC adsorbent and be expressed by using Eq. (9) as follow:

$$q_e = q_s \cdot \exp(-\beta \cdot \epsilon^2) \quad (9)$$

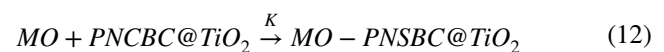
In this equation, q_s is the maximum adsorption capacity, β is the activity coefficient and it is used to measure the sorption energy E (kJ/mol), and ϵ is the Polanyi potential. The potential sorption energy and the Polanyi potential are illustrated by Eqs. (10) and (11), respectively:

$$\epsilon = RT \left(1 + \frac{1}{C_e} \right) \quad (10)$$

$$E = 1 / \sqrt{2\beta} \quad (11)$$

Therefore, based on the data shown in Table 5, the adsorption energy equals 2.59 kJ/mole. This suggests that the MO adsorption is physisorption onto 3% TiO₂@PNS-BC, with adsorption energy < 8 kJ/mole. Yet, the presence of various functional groups on the surface of the adsorbent, as confirmed by the FT–IR analysis, reveals that the possibility of occurrence of chemisorption cannot be neglected. The resulting data implies that the adsorption of MO onto the 3% TiO₂@PNS-BC adsorbent depends on the surface area of the studied adsorbent.

The adsorption of MO onto 3% TiO₂@PNS-BC was studied through four kinetics models: pseudo-first order (PFO), pseudo-second order (PSO), Elovich model, and Weber Morris model (Ezzati 2020; Machado et al. 2021; Wu et al. 2009). Figure 7b and Table 5 illustrate the relationship of q_t (mg/g) versus time (t , min) for MO adsorption on 3% TiO₂@PNS-BC and the calculated parameters for the four models. The obtained results indicate that R^2 value for the PSO model is the highest among the four models ($R^2 = 0.9531$). The resultant data demonstrate that adsorption rate of MO is affected by both dye and adsorbent concentrations, and can be expressed by Eq. (12):



On the other hand, R^2 values of the other models including Elovich and Weber Morris were significantly lower compared to PSO and PFO, and equals 0.8659, and 0.6188 for Elovich and Weber Morris, respectively, and these models cannot be used to describe the adsorption of MO on 3% TiO₂@PNS-BC.

Efficiency of the tested adsorbent compared to literature

Table S2 shows literature efforts for removing MO from wastewater using different biochar-based as well as synthetic adsorbents. The table shows these efforts arranged based on the q_{max} compared to the current investigation. Results

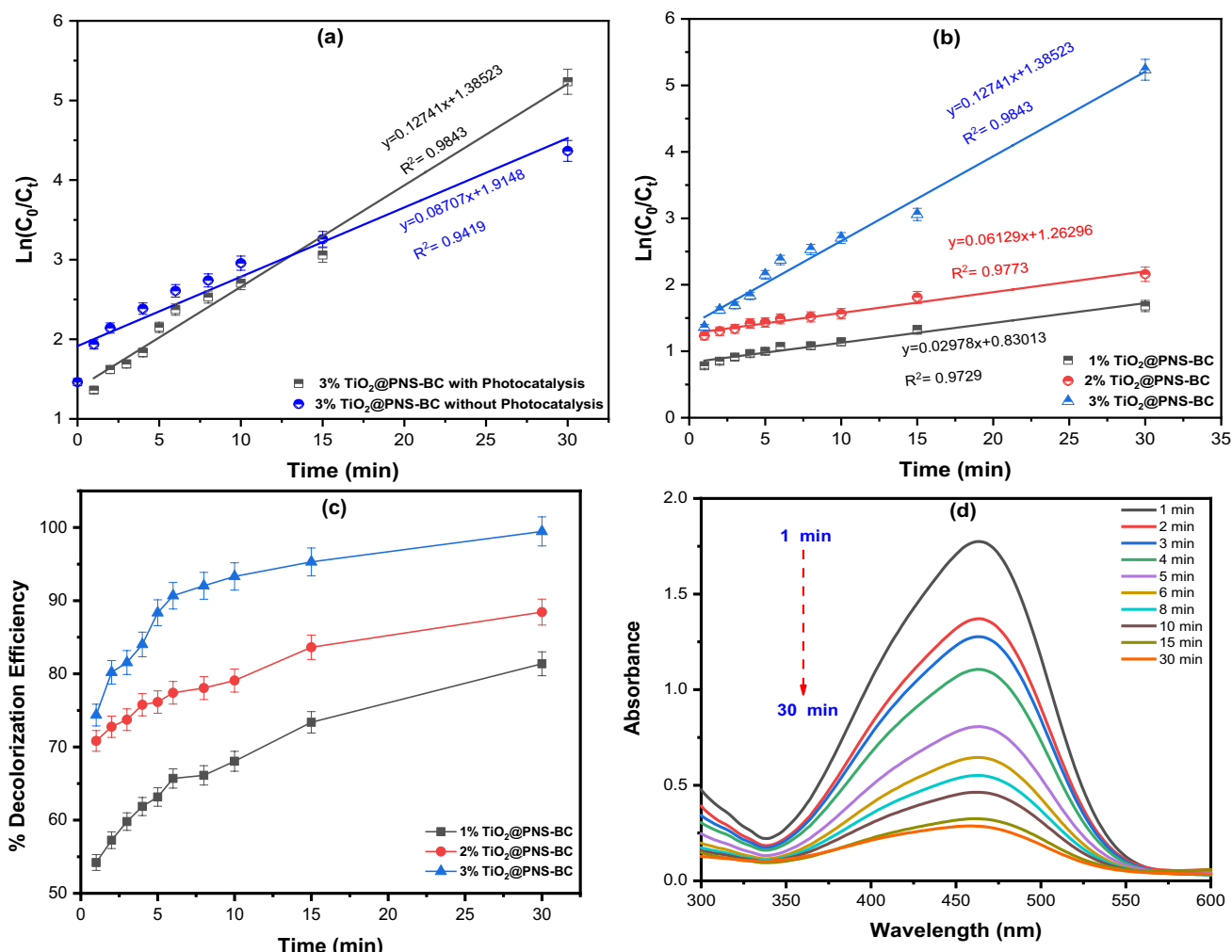


Fig. 8 **a** Photocatalytic decolorization kinetics of MO using 3% TiO₂@PNS-BC compared to the kinetics of a control experiment (only adsorption with no photocatalysis) over a period of 30 min, **b** Photocatalytic decolorization kinetics of MO over catalysts, **c** Photo-

catalytic degradation of MO using different concentrations of TiO₂, and **d** Absorption spectra of MO recorded over 30 min of UV-irradiation of MO-3% TiO₂@PNS-BC. Triplicate measurements are expressed using error bars

of the current approach indicate that 3% TiO₂@PNS-BC has the highest adsorption capacity (142.38 mg/g) when compared to other types of adsorbents (Ahmad et al. 2017; Annadurai et al. 2002; Bhatnagar et al. 2009; Cuong Nguyen et al. 2021; Loc et al. 2022; Sui et al. 2012; Yao et al. 2011; Yu et al. 2018).

Photocatalysis reaction kinetics

In the current investigation, photocatalysis was used to speed up the decolorization of MO. Adsorption kinetics together with the design optimization findings showed an almost 100% decolorization of MO could be achieved, however, after a period of 120 min of staying in contact with 3% TiO₂@PNS-BC. Investigation of photocatalysis kinetics

shows that with UV-irradiation of MO-3% TiO₂@PNS-BC, an almost complete decolorization of MO could be accomplished over a period of just 30 min. Figure 8a shows the photocatalysis reaction kinetics compared to the adsorption kinetics. Plots of $\ln(C_0/C_t)$ versus time (t , min) were fitted to the following first-order kinetics model given by Eq. (13).

$$\ln(C_0/C_t) = k_1 t \tag{13}$$

Where C_0 and C_t signify the initial [MO], and the [MO] after a certain irradiation time in case of photocatalysis or the equilibrium concentration following adsorption without photocatalysis, both expressed in ppm, k_1 is the rate constant (min^{-1}) calculated from the slope of the linear fit, and t is the time (min). A clear increase in the value of k_1 (min^{-1}) of the linear plots could be observed implying an increase in

the speed of the decolorization of MO using photocatalysis compared to adsorption alone. This control experiment shows a synergistic effect of the BC and TiO₂, where the existence of TiO₂ has accelerated the decolorization of MO, probably due to the anatase crystal form.

In this regard, the influence of increasing the concentration of the loaded TiO₂ (%TiO₂) on the BC surface on the photocatalysis kinetics was explored, Fig. 8b. As could be concluded comparing the slopes of the three curves (rate constants), 3% TiO₂@PNS-BC was the best catalyst compared to the 2% and the 1% counterparts with a decolorization rate constant of 0.12741 min⁻¹ which is almost 1.5× faster compared to the decolorization of MO using adsorption alone. These findings infer that the increased concentration of TiO₂ on the BC surface up to 3% implies an increase in the existence of the anatase crystal form, an issue which was also clearly reflected by the SEM micrographs where at a 3%, layers of TiO₂ exist on and almost completely cover the surface.

Comparing the 1% and 2% irradiated candidates. Figure 8b with the control experiment conducted without irradiation (adsorption alone), Fig. 8a, the rate constant has almost doubled, from 0.02978 min⁻¹ (1%—irradiated) to 0.06129 min⁻¹ (2%—irradiated) compared to 0.08707 min⁻¹ for a 3%—non-irradiated sample (adsorption only). These figures reflect the importance of finding the optimum concentration of TiO₂ (the preceding BB design optimization step). The lower performance of the 1% and 2%—irradiated samples compared to the adsorption only experiment could be attributed to the shelter effect of the biochar, where the excess biochar compared to the %TiO₂ could block the light reaching to the photocatalyst surface. Therefore, an optimum value of 3% TiO₂ is the best for the synthesis of the photocatalyst.

In the same itinerary, and in accord with the BB design output where 3% TiO₂@PNS-BC had the highest adsorptive efficiency, Fig. 8c shows that the highest decolorization efficiency (%DE) of MO could be achieved using 3% TiO₂@PNS-BC. Figure 8c shows that after 30 min, almost complete (99.47%) of MO could be recognized compared to 88.44% and 81.38% using the 2% and 1% commodities, respectively. Figure 8d shows the absorption spectra of MO recorded over 30 min of UV-irradiation of MO-3% TiO₂@PNS-BC. An obvious decrease in absorbance could be noted over time.

A comparison between the current MO decolorization efficiency in terms of the degradation rate constant, %DE, and the time consumed to achieve this %DE with the literature reported efforts is shown in Table 6 (Annadurai et al. 2002; Bhatnagar et al. 2009; Chen et al. 2011; Loc et al. 2022; Zhang et al. 2021). For the sake of a fair comparison, chosen efforts were all biochar-based investigations. Obtained data showed the superior performance of the 3% TiO₂@PNS-BC compared to the rest of catalysts. The rate constant (decolorization speed) was almost the highest with a %DE of 99.47% achieved over the shortest period, only 30 min.

Proposed adsorption/photocatalysis mechanism

Mechanism of the adsorption of MO onto 3% TiO₂@PNS-BC and the photocatalysis processes is summarized as in Fig. 9. The removal of MO from the solution could happen through different processes such as hydrogen bonding, electrostatic interaction, $\pi - \pi$ stacking, precipitation and ion exchange, Fig. 9. The $\pi - \pi$ stacking, for example, occurs between the aromatic ring of MO and the aromatic structure of the biochar. In addition, the electrostatic interaction could result from bonds being created between MO and the functional groups of TiO₂@PNS-BC as identified by the FT-IR

Table 6 A comparison of biochar-based photocatalysts for the decolorization of MO with the current approach

Photocatalyst	Rate constant (min ⁻¹)	%DE, time	References
3% TiO ₂ @PNS-BC	12.74 × 10 ⁻²	99.47%, 30 min	<i>Current work</i>
Ag/TiO ₂ /biochar (walnut shells)	6.29 × 10 ⁻²	97.48%, 60 min	(Shan et al. 2020)
TiO ₂	0.97 × 10 ⁻²	76.69%, 150 min	(Lu et al. 2019)
TiO ₂ /biochar (ratio: 0.2/1) (walnut shells)	2.26 × 10 ⁻²	96.88%, 150 min	
Biochar (corn cobs)	20.12 × 10 ⁻²	Not reported, 24 h	(Zhang et al. 2021)
β-FeOOH/Fe ₃ O ₄ /biochar	40.87 × 10 ⁻²	Not reported, 24 h	
Biochar (cornstalk)	0.23 × 10 ⁻²	85.4%, 60 min	(Jiang and Liu 2023)
Cornstalk biochar-TiO ₂ (ratio: 0.75:1)	5.10 × 10 ⁻²	97.1%, 60 min	
Wood-based biochar- Cu ₂ O nanoparticles	21.85 × 10 ⁻³	94.5% (20 mg/L), 140 min	(Zhang et al. 2023)
CdS-WPB (wood powder biochar)-g-C ₃ N ₄	9.00 × 10 ⁻²	99%, 80 min	(Ma et al. 2023)

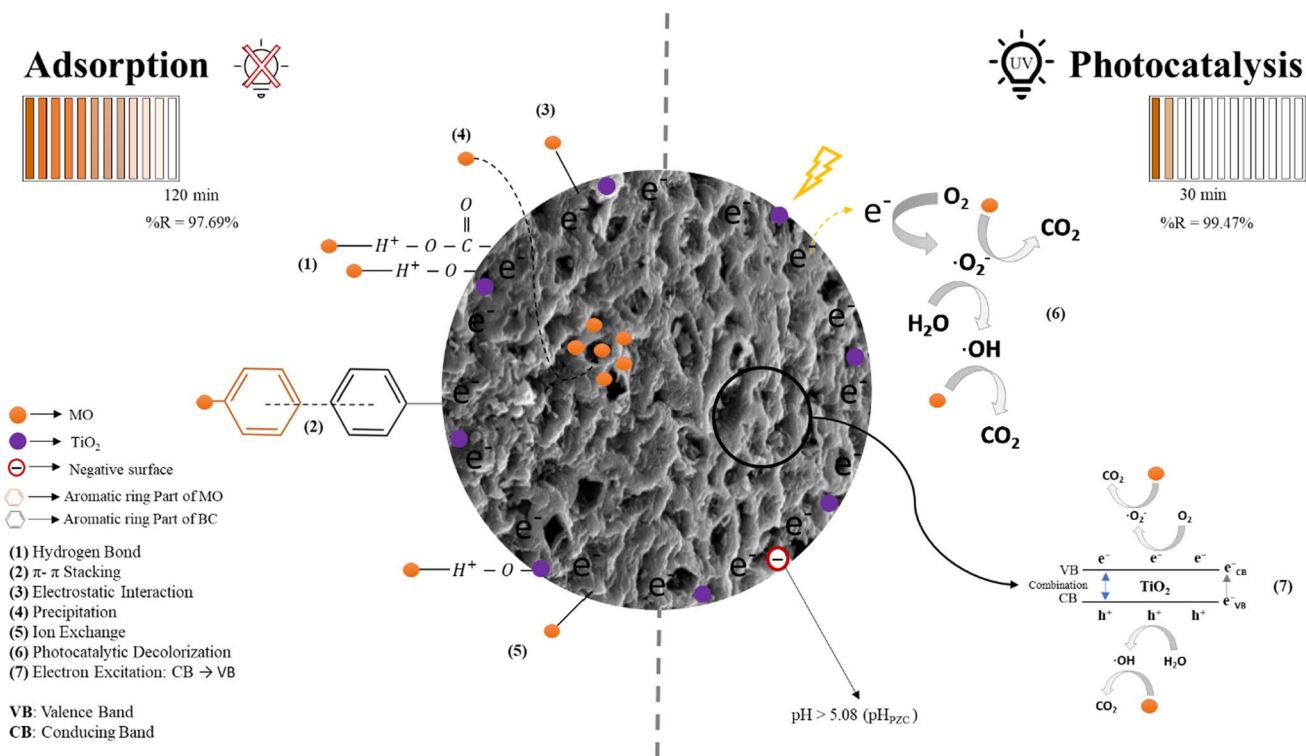


Fig. 9 Possible mechanism of adsorption/photocatalysis of MO onto 3% TiO₂@PNS-BC surface

analysis. The surface of 3% TiO₂@PNS-BC is negatively charged, given that the pHPZC is 5.08, lower than the solution pH (pH = 6.00 ± 0.20). The charge difference between the surface of the studied adsorbent and MO, coupled with the high surface area of the adsorbent, supports the applicability of both chemisorption and physisorption mechanisms in discussing the adsorption of MO onto 3% TiO₂@PNS-BC. On the other hand, photocatalytic degradation happens by exciting the electrons on the surface through the exposure to the ultraviolet (UV) radiation. The electron in valence band (VB) gets excited to conduction band (CB) upon absorption of a suitable wavelength of light, in this case UV light, and the distance between VB and CB is known as the band gap. Therefore, the minimum energy required for excitation of an electron is equal to the energy of the band gap.

Selectivity of the prepared binary composites

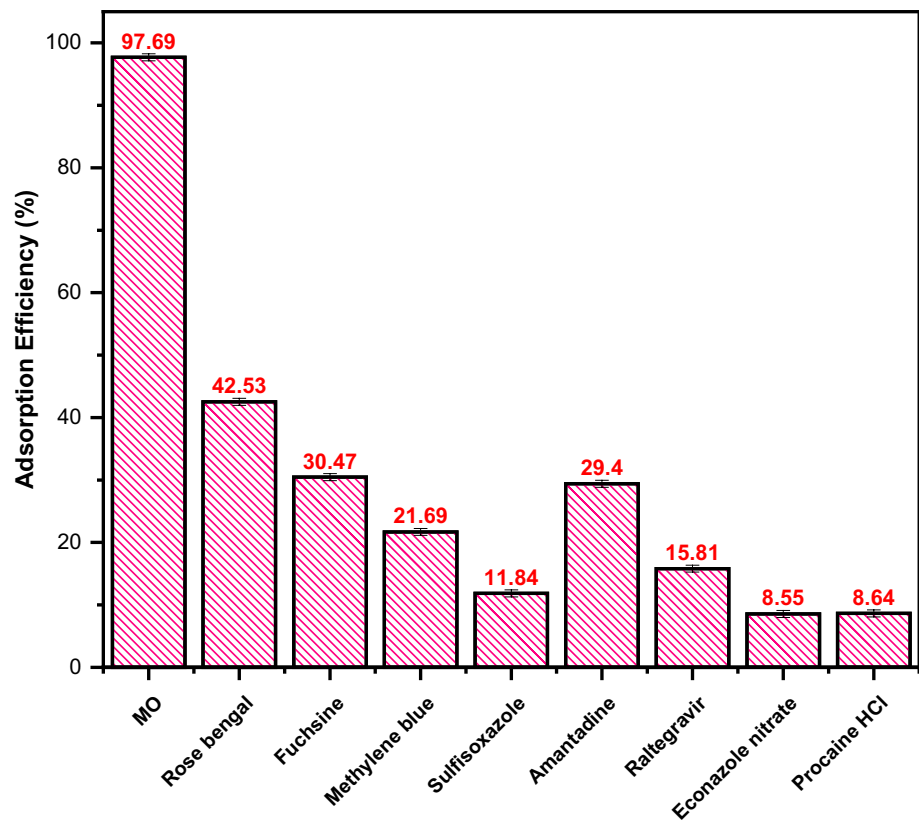
To investigate the binding specificity, the adsorption effectiveness of 3% TiO₂@PNS-BC was tested for in nine different aqueous solutions of MO, methylene blue, rose bengal, fuchsine, sulfisoxazole, amantadine, raltegravir, econazole nitrate, and procaine HCl, all at a concentration of 50 ppm and under the same optimal adsorption conditions for MO removal as determined by the BB design. As shown in Fig. 10, the results demonstrate that 3% TiO₂@PNS-BC exhibits a significant adsorption efficiency toward MO,

with a removal efficiency of 97.69% compared to 42.53%, 30.47%, 29.40%, and 21.69% toward rose bengal, fuchsine, amantadine, and methylene blue, respectively. The %R of the remaining compounds was less than 16%, indicating the low preference of 3% TiO₂@PNS-BC for adsorbing these compounds compared to MO.

Conclusion

According to the obtained data, recycling pistachio nutshells can create efficient and cost-effective biochar-based adsorbent. Numerous characterization techniques were applied on both PNS-BC and TiO₂@PNS-BC for the determination of the structure and morphology of both. Among the tested adsorbents, the 3% TiO₂@PNS-BC showed a better adsorption efficiency compared to PNS-BC, 3% TiO₂@PNS-BC had larger surface area (33.37 m²/g) and smaller pore size (0.028 cm³/g). BB design was used to maximize the removal efficiency of the TiO₂@PNS-BC as a function of five variables. The aim was to minimize the usage of chemicals and resources while maximizing MO removal. In design analysis, pH had the lowest influence on the response compared to %TiO₂, AD, RT, and [MO]. While squared effect of %TiO₂ (AA) had the highest effect. Equilibrium studies showed that the obtained results matched Langmuir isotherm, and that

Fig. 10 Adsorption selectivity of 3% TiO₂@PNS-BC toward MO compared to other pharmaceuticals and dyes



the adsorption process is favorable and spontaneous with $q_{\max} = 142.38$ mg/g. Investigation of adsorption kinetics showed that PSO model perfectly matched the adsorption of MO onto 3% TiO₂@PNS-BC indicating that the process was physisorption with sorption energy of 2.59 kJ/mole. Therefore, 3% TiO₂@PNS-BC can be utilized as effective adsorbent for the removal of MO from aqueous solutions. Additionally, photocatalytic decolorization experiment data shows that after 30 min, almost complete removal (99.47%) of MO could be recognized compared to 88.44% and 81.38% using the 2% and 1% commodities, respectively.

Supplementary Information The online version contains supplementary material available at <https://doi.org/10.1007/s13201-023-02035-9>.

Acknowledgments The project members would like to extend their special thanks to the Central Lab Unit (CLU) at Qatar University.

Funding This publication was supported by Qatar University Student Grant [QUST-1-CAS-2023-854]. The findings achieved herein are solely the responsibility of the authors.

Declarations

Conflict of interest The authors declare no conflict of interest.

Ethical approval This article does not contain any studies with animals and human subjects. The authors confirm that the whole study

meets the ethical guidelines and adheres to the legal requirements of the study country.

Consent to participate No informed consent was needed.

Consent for publication All authors express their consent for the publication of this article.

Open Access This article is licensed under a Creative Commons Attribution 4.0 International License, which permits use, sharing, adaptation, distribution and reproduction in any medium or format, as long as you give appropriate credit to the original author(s) and the source, provide a link to the Creative Commons licence, and indicate if changes were made. The images or other third party material in this article are included in the article's Creative Commons licence, unless indicated otherwise in a credit line to the material. If material is not included in the article's Creative Commons licence and your intended use is not permitted by statutory regulation or exceeds the permitted use, you will need to obtain permission directly from the copyright holder. To view a copy of this licence, visit <http://creativecommons.org/licenses/by/4.0/>.

References

- Ahmad A, Razali MH, Mamat M, Mehamod FSB, Anuar Mat Amin K (2017) Adsorption of methyl orange by synthesized and functionalized-CNTs with 3-aminopropyltriethoxysilane loaded TiO₂ nanocomposites. *Chemosphere* 168:474–482. <https://doi.org/10.1016/j.chemosphere.2016.11.028>

- Akazdam S, Chafi M, Sebbahi L, Benchekroune R, Gourich B, Barka N (2018) Decolorization of acid orange 7 dye from aqueous solution by adsorption on naoh treated eggshells in continuous fixed bed reactor application using response surface methodology: optimization by box-behnken design. *Moroc J Chem* 6(4):6–4
- Alardhi SM, Fiyadh SS, Salman AD, Adelikhah M (2023) Prediction of methyl orange dye (MO) adsorption using activated carbon with an artificial neural network optimization modeling. *Heliyon* 9(1):e12888. <https://doi.org/10.1016/j.heliyon.2023.e12888>
- Aljuaid A, Almeahadi M, Alsaiari AA, Allahyani M, Abdulaziz O, Alsharif A, Khan I (2023) g-C(3)N(4) based photocatalyst for the efficient photodegradation of toxic methyl orange dye: recent modifications and future perspectives. *Molecules* 28(7):3199. <https://doi.org/10.3390/molecules28073199>
- Andas J, Wazil N (2019) From waste mango kernel into high surface area activated carbon. *Mater Today Proc* 19:1541–1546. <https://doi.org/10.1016/j.matpr.2019.11.181>
- Annadurai G, Juang R-S, Lee D-J (2002) Use of cellulose-based wastes for adsorption of dyes from aqueous solutions. *J Hazard Mater* 92(3):263–274. [https://doi.org/10.1016/S0304-3894\(02\)00017-1](https://doi.org/10.1016/S0304-3894(02)00017-1)
- Antonio-Cisneros CM, Dávila-Jiménez MM, Elizalde-González MP, García-Díaz E (2015) TiO₂ immobilized on manihot carbon: optimal preparation and evaluation of its activity in the decomposition of indigo carmine. *Int J Mol Sci* 16(1):1590–1612
- Araújo CST, Almeida ILS, Rezende HC, Marcionilio SMLO, León JLL, de Matos TN (2018) Elucidation of mechanism involved in adsorption of Pb(II) onto lobeira fruit (*solanum lycocarpum*) using Langmuir, Freundlich and Temkin isotherms. *Microchem J* 137:348–354. <https://doi.org/10.1016/j.microc.2017.11.009>
- Babić BM, Milonjić SK, Polovina MJ, Kaludierović BV (1999) Point of zero charge and intrinsic equilibrium constants of activated carbon cloth. *Carbon* 37(3):477–481. [https://doi.org/10.1016/S0008-6223\(98\)00216-4](https://doi.org/10.1016/S0008-6223(98)00216-4)
- Beams R, Gustavo Cançado L, Novotny L (2015) Raman characterization of defects and dopants in graphene. *J Phys Condens Matter* 27(8):083002. <https://doi.org/10.1088/0953-8984/27/8/083002>
- Bhatnagar A, Kumar E, Minocha AK, Jeon B-H, Song H, Seo Y-C (2009) Removal of anionic dyes from water using citrus limonum (Lemon) peel: equilibrium studies and kinetic modeling. *Sep Sci Technol* 44(2):316–334. <https://doi.org/10.1080/01496390802437461>
- Box GEP, Behnken DW (1960) Some new three level designs for the study of quantitative variables. *Technometrics* 2(4):455–475. <https://doi.org/10.1080/00401706.1960.10489912>
- Cantarella M, Carroccio SC, Dattilo S, Avolio R, Castaldo R, Puglisi C, Privitera V (2019) Molecularly imprinted polymer for selective adsorption of diclofenac from contaminated water. *Chem Eng J* 367:180–188. <https://doi.org/10.1016/j.cej.2019.02.146>
- Chen Z-X, Jin X-Y, Chen Z, Megharaj M, Naidu R (2011) Removal of methyl orange from aqueous solution using bentonite-supported nanoscale zero-valent iron. *J Coll Interf Sci* 363(2):601–607. <https://doi.org/10.1016/j.jcis.2011.07.057>
- Cuong Nguyen X, Nguyen TH et al (2021) Sustainable carbonaceous biochar adsorbents derived from agro-wastes and invasive plants for cation dye adsorption from water. *Chemosphere* 282:131009. <https://doi.org/10.1016/j.chemosphere.2021.131009>
- Da Dalt S, Alves AK, Bergmann CP (2013) Photocatalytic degradation of methyl orange dye in water solutions in the presence of MWCNT/TiO₂ composites. *Mater Res Bull* 48(5):1845–1850. <https://doi.org/10.1016/j.materresbull.2013.01.022>
- Dai N, Yi S, Zhang X, Feng L, Ding H, Song D, Zhang Y (2023) Typical synthesis of an iron-modified laponite @ diatomite composite for photo-fenton degradation of methyl orange dyes. *Appl Surf Sci* 607:154886. <https://doi.org/10.1016/j.apsusc.2022.154886>
- El Amri A, Kadiri L, Hsissou R, Lebkiri A, Wardighi Z, Rifi EH, Lebkiri A (2023) Investigation of typha latifolia (TL) as potential biosorbent for removal of the methyl orange anionic dye in the aqueous solution. kinetic and DFT approaches. *J Mol Struct* 1272:134098. <https://doi.org/10.1016/j.molstruc.2022.134098>
- Elamin NY, Modwi A, Abd El-Fattah W, Rajeh A (2023) Synthesis and structural of Fe₃O₄ magnetic nanoparticles and its effect on the structural optical, and magnetic properties of novel poly(methyl methacrylate)/ Polyaniline composite for electromagnetic and optical applications. *Opt Mater* 135:113323. <https://doi.org/10.1016/j.optmat.2022.113323>
- El-Azazy M, El-Shafie AS, Ashraf A, Issa AA (2019a) Eco-structured biosorbent removal of basic fuchsin using pistachio nutshells: a definitive screening design—based approach. *Appl Sci* 9(22):4855
- El-Azazy M, Kalla RN, Issa AA, Al-Sulaiti M, El-Shafie AS, Shomar B, Al-Saad K (2019b) Pomegranate peels as versatile adsorbents for water purification: application of box-behnken design as a methodological optimization approach. *Environ Prog Sustain Energy* 38(6):13223. <https://doi.org/10.1002/ep.13223>
- El-Azazy M, El-Shafie AS, Al-Shaikh Yousef B (2021a) Green tea waste as an efficient adsorbent for methylene blue: structuring of a novel adsorbent using full factorial design. *Molecules* 26(20):6138. <https://doi.org/10.3390/molecules26206138>
- El-Azazy M, El-Shafie AS, Morsy H (2021b) Biochar of spent coffee grounds as per se and impregnated with TiO₂: promising waste-derived adsorbents for balofloxacin. *Molecules* 26(8):2295
- El-Azazy M, El-Shafie AS, Al-Mulla R, Hassan SS, Nimir HI (2023) Enhanced adsorptive removal of rifampicin and tigecycline from single system using nano-ceria decorated biochar of mango seed kernel. *Heliyon* 9(5):e15802. <https://doi.org/10.1016/j.heliyon.2023.e15802>
- El-Shafie AS, Hassan SS, Akther N, El-Azazy M (2021) Watermelon rinds as cost-efficient adsorbent for acridine orange: a response surface methodological approach. *Environ Sci Pollut Res*. <https://doi.org/10.1007/s11356-021-13652-9>
- El-Shafie AS, Barah FG, Abouseada M, El-Azazy M (2023) Performance of pristine versus magnetized orange peels biochar adapted to adsorptive removal of daunorubicin: eco-structuring. *Kinet Equilib Stud* 13(9):1444
- Ezzati R (2020) Derivation of pseudo-first-order, pseudo-second-order and modified pseudo-first-order rate equations from langmuir and freundlich isotherms for adsorption. *Chem Eng J* 392:123705. <https://doi.org/10.1016/j.cej.2019.123705>
- Farhan A, Ismail A, Abed B (2021) Applying box-behnken design with statistical optimization for removal vat orange dye from aqueous solution using kaolin. *J Eng Sci Technol* 16:1588–1600
- Fazal T, Razzaq A, Javed F, Hafeez A, Rashid N, Amjad US, Rehman F (2020) Integrating adsorption and photocatalysis: a cost effective strategy for textile wastewater treatment using hybrid biochar-TiO₂ composite. *J Hazard Mater* 390:121623. <https://doi.org/10.1016/j.jhazmat.2019.121623>
- Fernández-Ibáñez P, Polo-López MI, Malato S, Wadhwa S, Hamilton JWJ, Dunlop PSM, Byrne JA (2015) Solar photocatalytic disinfection of water using titanium dioxide graphene composites. *Chem Eng J* 261:36–44. <https://doi.org/10.1016/j.cej.2014.06.089>
- Ferreira SLC, Bruns RE, Ferreira HS, Matos GD, David JM, Brandão GC, dos Santos WNL (2007) Box-behnken design: an alternative for the optimization of analytical methods. *Anal Chimica Acta* 597(2):179–186. <https://doi.org/10.1016/j.aca.2007.07.011>
- Fito J, Kefeni KK, Nkambule TTI (2022) The potential of biochar-photocatalytic nanocomposites for removal of organic micropollutants from wastewater. *Sci Total Environ* 829:154648. <https://doi.org/10.1016/j.scitotenv.2022.154648>
- Foo KY, Hameed BH (2011) Preparation and characterization of activated carbon from pistachio nut shells via microwave-induced

- chemical activation. *Biomass Bioenergy* 35(7):3257–3261. <https://doi.org/10.1016/j.biombioe.2011.04.023>
- Ganesapillai M, Mehta R, Tiwari A, Sinha A, Bakshi HS, Chellappa V, Drewnowski J (2023) Waste to energy: a review of biochar production with emphasis on mathematical modelling and its applications. *Heliyon* 9(4):e14873. <https://doi.org/10.1016/j.heliyon.2023.e14873>
- Goel PK (2006) Water pollution: causes, effects and control. New age international. <https://books.google.com.qa/books?id=4R9CY YoiFCcC>
- Guo X, Wang J (2019) Comparison of linearization methods for modeling the langmuir adsorption isotherm. *J Mol Liq* 296:111850. <https://doi.org/10.1016/j.molliq.2019.111850>
- Haque E, Lee JE, Jang IT, Hwang YK, Chang JS, Jegal J, Jung SH (2010) Adsorptive removal of methyl orange from aqueous solution with metal-organic frameworks, porous chromium-benzenedicarboxylates. *J Hazard Mater*. <https://doi.org/10.1016/j.jhazmat.2010.05.047>
- Hidayat D, Lestari WW, Dendy D, Khoerunnisa F, Handayani M, Sanjaya EH, Gunawan T (2023) Adsorption studies of anionic and cationic dyes on MIL-100(Cr) synthesized using facile and green mechanochemical method. *J Inorg Organomet Polym Mater*. <https://doi.org/10.1007/s10904-023-02569-0>
- Irani E, Amoli-Diva M (2020) Hybrid adsorption–photocatalysis properties of quaternary magneto-plasmonic ZnO/MWCNTs nanocomposite for applying synergistic photocatalytic removal and membrane filtration in industrial wastewater treatment. *J Photochem Photobiol A Chem* 391:112359. <https://doi.org/10.1016/j.jphotochem.2020.112359>
- Iwuozor KO, Ighalo JO, Emenike EC, Ogunfowora LA, Igwegbe CA (2021) Adsorption of methyl orange: a review on adsorbent performance. *Curr Res Green Sustain Chem* 4:100179. <https://doi.org/10.1016/j.crgsc.2021.100179>
- Jiang Y, Liu A (2023) Cornstalk biochar-TiO₂ composites as alternative photocatalyst for degrading methyl orange. *Environ Sci Pollut Res* 30(11):31923–31934. <https://doi.org/10.1007/s11356-022-24490-8>
- Langmuir D, Herman JS (1980) The mobility of thorium in natural waters at low temperatures. *Geochim Et Cosmochim Acta* 44(11):1753–1766. [https://doi.org/10.1016/0016-7037\(80\)90226-4](https://doi.org/10.1016/0016-7037(80)90226-4)
- Leng Q, Xu S, Wu X, Wang S, Jin D, Wang P, Dong F (2022) Electrochemical removal of synthetic methyl orange dyeing wastewater by reverse electro dialysis reactor: experiment and mineralizing model. *Environ Res* 214:114064. <https://doi.org/10.1016/j.envres.2022.114064>
- León A, Reuquen P, Garín C, Segura R, Vargas P, Zapata P, Orihuela PA (2017) FTIR and Raman characterization of TiO₂ nanoparticles coated with polyethylene glycol as carrier for 2-methoxyestradiol. *Appl Sci* 7(1):49
- Li X, Chen J, Wang Y, Cheng Z, Chen X, Gao X, Guo M (2023) Porous spherical Cu₂O supported by wood-based biochar skeleton for the adsorption-photocatalytic degradation of methyl orange. *Appl Surf Sci* 611:155744. <https://doi.org/10.1016/j.apsusc.2022.155744>
- Lim T-T, Yap P-S, Srinivasan M, Fane AG (2011) TiO₂/AC composites for synergistic adsorption-photocatalysis processes: present challenges and further developments for water treatment and reclamation. *Crit Rev Environ Sci Technol* 41(13):1173–1230. <https://doi.org/10.1080/10643380903488664>
- Lo Bello G, Bartoli M, Giorcelli M, Rovere M, Tagliaferro A (2022) A review on the use of biochar derived carbon quantum dots production for sensing applications. *Biosensors* 10(3):117
- Loc NX, Tuyen PTT, Mai LC, Phuong DTM (2022) Chitosan-modified biochar and unmodified biochar for methyl orange: adsorption characteristics and mechanism exploration. *Toxics* 10(9):500
- Lu L, Shan R, Shi Y, Wang S, Yuan H (2019) A novel TiO₂/biochar composite catalysts for photocatalytic degradation of methyl orange. *Chemosphere* 222:391–398. <https://doi.org/10.1016/j.chemosphere.2019.01.132>
- Lu Y, Cai Y, Zhang S, Zhuang L, Hu B, Wang S, Wang X (2022) Application of biochar-based photocatalysts for adsorption-(photo)degradation/reduction of environmental contaminants: mechanism, challenges and perspective. *Biochar* 4(1):45. <https://doi.org/10.1007/s42773-022-00173-y>
- Luo Y, Wei X, Gao B, Zou W, Zheng Y, Yang Y, Dong L (2019) Synergistic adsorption-photocatalysis processes of graphitic carbon nitrate (g-C₃N₄) for contaminant removal: kinetics, models, and mechanisms. *Chem Eng J* 375:122019. <https://doi.org/10.1016/j.cej.2019.122019>
- Ma C, Zhang Y, Yin B, Chen J, Guo M, Gao X (2023) Wood powder biochar in CdS-WPB-g-C₃N₄ heterojunction as an electron transfer medium for enhancing photocatalytic performance toward degradation methyl orange. *J Environ Chem Eng* 11(1):109135. <https://doi.org/10.1016/j.jece.2022.109135>
- Machado DB, Skoronski E, Soares C, Padoin N (2021) Immobilisation of phosphonium-based ionic liquid in polysulfone capsules for the removal of phenolic compounds, with an emphasis on 2,4-dichlorophenol, in aqueous solution. *J Environ Manag* 291:112670. <https://doi.org/10.1016/j.jenvman.2021.112670>
- El-Azazy M, El-Shafie AS, Al-Saad K (2022) Application of infrared spectroscopy in the characterization of lignocellulosic biomasses utilized in wastewater treatment, Chap 8. In: El-Azazy M, Al-Saad K, El-Shafie AS (eds), *Infrared Spectroscopy*. IntechOpen. <https://doi.org/10.5772/intechopen.108878>
- Moussavi G, Barikbin B (2010) Biosorption of chromium(VI) from industrial wastewater onto pistachio hull waste biomass. *Chem Eng J* 162(3):893–900. <https://doi.org/10.1016/j.cej.2010.06.032>
- Mugundan S, Rajamannan B, Viruthagiri G, Shanmugam N, Gobi R, Praveen P (2015) Synthesis and characterization of undoped and cobalt-doped TiO₂ nanoparticles via sol–gel technique. *Appl Nanosci* 5(4):449–456. <https://doi.org/10.1007/s13204-014-0337-y>
- Osman AI, Fawzy S, Farghali M, El-Azazy M, Elgarahy AM, Fahim RA, Rooney DW (2022) Biochar for agronomy, animal farming, anaerobic digestion, composting, water treatment, soil remediation, construction, energy storage, and carbon sequestration: a review. *Environ Chem Lett* 20(4):2385–2485. <https://doi.org/10.1007/s10311-022-01424-x>
- Owa FD (2013) Water pollution: sources, effects, control and management. *Mediterranean J Soc Sci* 4(8):65
- Pang YL, Law ZX, Lim S, Chan YY, Shuit SH, Chong WC, Lai CW (2021) Enhanced photocatalytic degradation of methyl orange by coconut shell–derived biochar composites under visible LED light irradiation. *Environ Sci Pollut Res* 28(21):27457–27473. <https://doi.org/10.1007/s11356-020-12251-4>
- Pravakar O, Siddaiah T, Ramacharyulu PVRK, Gopal NO, Ramu C, Nagabhushana H (2021) Studies on the effect of Cu doping on the structural, thermal and spectroscopic properties of PVA/MAA:EA polyblend films. *Mater Res Innov* 25(7):442–448. <https://doi.org/10.1080/14328917.2020.1831152>
- Qiao D, Li Z, Duan J, He X (2020) Adsorption and photocatalytic degradation mechanism of magnetic graphene oxide/ZnO nanocomposites for tetracycline contaminants. *Chem Eng J* 400:125952. <https://doi.org/10.1016/j.cej.2020.125952>
- Shan R, Lu L, Gu J, Zhang Y, Yuan H, Chen Y, Luo B (2020) Photocatalytic degradation of methyl orange by Ag/TiO₂/biochar composite catalysts in aqueous solutions. *Mater Sci Semiconductor Process* 114:105088. <https://doi.org/10.1016/j.mssp.2020.105088>

- Shi W, Ren H, Huang X, Li M, Tang Y, Guo F (2020) Low cost red mud modified graphitic carbon nitride for the removal of organic pollutants in wastewater by the synergistic effect of adsorption and photocatalysis. *Sep Purif Technol* 237:116477. <https://doi.org/10.1016/j.seppur.2019.116477>
- Sui K, Li Y, Liu R, Zhang Y, Zhao X, Liang H, Xia Y (2012) Biocomposite fiber of calcium alginate/multi-walled carbon nanotubes with enhanced adsorption properties for ionic dyes. *Carbohydr Polym* 90(1):399–406. <https://doi.org/10.1016/j.carbpol.2012.05.057>
- Tripathi P, Srivastava VC, Kumar A (2009) Optimization of an azo dye batch adsorption parameters using Box-behnken design. *Desalination* 249(3):1273–1279. <https://doi.org/10.1016/j.desal.2009.03.010>
- Wang G, Liu Y, Ye J, Lin Z, Yang X (2020a) Electrochemical oxidation of methyl orange by a Magnéli phase Ti_4O_7 anode. *Chemosphere* 241:125084. <https://doi.org/10.1016/j.chemosphere.2019.125084>
- Wang W, Zhang J, Chen T, Sun J, Ma X, Wang Y, Xie Z (2020b) Preparation of TiO_2 -modified biochar and its characteristics of photo-catalysis degradation for enrofloxacin. *Sci Rep* 10(1):6588. <https://doi.org/10.1038/s41598-020-62791-5>
- Wang X, Liu X, Yuan F, Wang B, Peng Q (2023) Selective decolorization of methylene blue from methyl orange in heterogeneous fenton-like reaction. *Int J Environ Res* 17(1):17. <https://doi.org/10.1007/s41742-023-00509-x>
- Wu F-C, Tseng R-L, Juang R-S (2009) Characteristics of elovich equation used for the analysis of adsorption kinetics in dye-chitosan systems. *Chem Eng J* 150(2):366–373. <https://doi.org/10.1016/j.cej.2009.01.014>
- Yao Y, Bing H, Feifei X, Xiaofeng C (2011) Equilibrium and kinetic studies of methyl orange adsorption on multiwalled carbon nanotubes. *Chem Eng J* 170(1):82–89. <https://doi.org/10.1016/j.cej.2011.03.031>
- Yu S, Yun HJ, Kim YH, Yi J (2014) Carbon-doped TiO_2 nanoparticles wrapped with nanographene as a high performance photocatalyst for phenol degradation under visible light irradiation. *Appl Catal B Environ* 144:893–899. <https://doi.org/10.1016/j.apcatb.2013.08.030>
- Yu J, Zhang X, Wang D, Li P (2018) Adsorption of methyl orange dye onto biochar adsorbent prepared from chicken manure. *Water Sci Technol* 77(5):1303–1312. <https://doi.org/10.2166/wst.2018.003>
- Yu F, Tian F, Zou H, Ye Z, Peng C, Huang J, Gao B (2021) ZnO/biochar nanocomposites via solvent free ball milling for enhanced adsorption and photocatalytic degradation of methylene blue. *J Hazard Mater* 415:125511. <https://doi.org/10.1016/j.jhazmat.2021.125511>
- Yu H, Cai D, Li S, Gao C, Xue L (2023) Tight UF membranes with ultrahigh water flux prepared by in-situ growing ZIF particles in NIPS process for greatly enhanced dye removal efficiency. *J Membr Sci* 666:121136. <https://doi.org/10.1016/j.memsci.2022.121136>
- Zhang Z, Wang G, Li W, Zhang L, Guo B, Ding L, Li X (2021) Photocatalytic activity of magnetic nano- β -FeOOH/ $Fe_{(3)}O_{(4)}$ /biochar composites for the enhanced degradation of methyl orange under visible light. *Nanomaterials* 11(2):526. <https://doi.org/10.3390/nano11020526>
- Zhang L, Xiao C, Li Z, Guo J, Du G, Cheng X, Jia Y (2023) Degradation of methyl orange using persulfate activated by magnetic CuS/Fe₃O₄ catalyst: catalytic performance and mechanisms. *Appl Surf Sci* 618:156595. <https://doi.org/10.1016/j.apsusc.2023.156595>

Publisher's Note Springer Nature remains neutral with regard to jurisdictional claims in published maps and institutional affiliations.